



## Lagrangian and Eulerian analysis of transport and mixing in the three dimensional, time dependent Hill's spherical vortex

Kevin L. McIlhany, Stephen Guth, and Stephen Wiggins

Citation: Physics of Fluids **27**, 063603 (2015); doi: 10.1063/1.4922539

View online: <http://dx.doi.org/10.1063/1.4922539>

View Table of Contents: <http://scitation.aip.org/content/aip/journal/pof2/27/6?ver=pdfcov>

Published by the AIP Publishing

---

### Articles you may be interested in

[Global and Koopman modes analysis of sound generation in mixing layers](#)  
Phys. Fluids **25**, 124101 (2013); 10.1063/1.4834438

[Viscous and inviscid spatial stability analysis of compressible swirling mixing layers](#)  
Phys. Fluids **20**, 114103 (2008); 10.1063/1.2931591

[Three-dimensional acoustic scattering by vortical flows. II. Axisymmetric scattering by Hill's spherical vortex](#)  
Phys. Fluids **13**, 2890 (2001); 10.1063/1.1401815

[Mixing in two-dimensional vortex interactions](#)  
Phys. Fluids **12**, 3285 (2000); 10.1063/1.1320838

[Growth of large scale structures in two-dimensional mixing layers](#)  
Phys. Fluids **9**, 2168 (1997); 10.1063/1.869339

---



# Lagrangian and Eulerian analysis of transport and mixing in the three dimensional, time dependent Hill's spherical vortex

Kevin L. McIlhany,<sup>1,a)</sup> Stephen Guth,<sup>2,b)</sup> and Stephen Wiggins<sup>3,c)</sup>

<sup>1</sup>*Physics Department, U. S. Naval Academy, Stop 9c, 572c Holloway RD, Annapolis, Maryland 21402-5002, USA*

<sup>2</sup>*Mathematics Department, U. S. Naval Academy, Stop 9c, 572c Holloway RD, Annapolis, Maryland 21402-5002, USA*

<sup>3</sup>*School of Mathematics, University of Bristol, University Walk, Bristol BS8 1TW, United Kingdom*

(Received 13 January 2015; accepted 2 June 2015; published online 18 June 2015)

In this paper, we extend the notion of Eulerian indicators (EIs), previously developed for two dimensional time dependent flows, to three dimensional time dependent flows, where the time dependence can be arbitrary. These are applied to a study of transport and mixing in the Hill's spherical vortex subject to a linear strain rate field. We consider the axisymmetric case and the fully three dimensional case with different types of time dependence. We develop a Lagrangian characterization of transport and mixing appropriate for open three dimensional flows and we show that the EIs provide a detailed description of the flow structure that can be correlated with the Lagrangian transport and mixing results. The EIs yield results consistent with the dynamics of the Hill's vortex flow characteristics, correlation with transverse shear, and anti-correlation with transversality. © 2015 AIP Publishing LLC.  
[<http://dx.doi.org/10.1063/1.4922539>]

## I. INTRODUCTION

The dynamical systems approach to Lagrangian transport and mixing in fluid mechanics is now well established. There are now many discussions of the development of this topic. The paper of Aref<sup>1</sup> is an excellent source for background and history. In particular, it noted the important papers of Arnold<sup>2</sup> and Hénon<sup>3</sup> which, in some sense, were 20 yr ahead of their time. Other relevant reviews, collections of papers, and books are Refs. 4–11.

Even though transport and mixing are inherently Lagrangian in nature (i.e., they are phenomena that are concerned with “where particles go”), the ubiquity and advantages of the Eulerian point of view motivate efforts to provide an explanation for these Lagrangian phenomena. Indeed, early in the development of the subject, Ottino<sup>12</sup> noted that “streamline crossing” appears to promote good mixing and, later on, Villermieux, Stroock, and Stone<sup>13</sup> observed that transversely oriented shears appeared to promote good mixing in certain channel or duct flows. Both of these observations were Eulerian in nature, but they are embodied in the mathematical definition of two dimensional linked twist maps (LTMs).<sup>10,11,14,15</sup> This is one of the rare dynamical systems where it is possible to give precise conditions for the map to possess the rigorous mathematical property of “strong mixing” on the entire domain of the map (i.e., on a set of “full measure”). Building on this analogy, Sturman and Wiggins<sup>16</sup> introduced the notion of “Eulerian indicators” (EIs), which are quantities for measuring the amount of “streamline crossing” and “transversely oriented shear” in classes of flows that could

---

<sup>a)</sup>[mcilhany@usna.edu](mailto:mcilhany@usna.edu)

<sup>b)</sup>[guth@usna.edu](mailto:guth@usna.edu)

<sup>c)</sup>[s.wiggins@bristol.ac.uk](mailto:s.wiggins@bristol.ac.uk)

be modeled as two dimensional maps having the characteristics of LTM<sub>s</sub>. In particular, these are two dimensional flows “blinking in time” (e.g., the Aref blinking vortex flow) or three dimensional, spatially periodic, steady flows, where the map is constructed by considering the evolution of trajectories from the beginning to the end of each spatial period (“blinking in space”), e.g., the partitioned pipe mixer.

Sturman and Wiggins<sup>16</sup> developed EI<sub>s</sub> that quantified the extent of (averaged) “streamline crossing,” (averaged) shear rate, and the (averaged) product of these two EI<sub>s</sub> (thus quantifying the notion of “transversely oriented shear”). They applied these EI<sub>s</sub> to four different two dimensional “blinking flows”—the Aref blinking vortex flow, the “separatrix model,” the pulsed source-sink pair flow, and the partitioned pipe mixer. For these flows, they showed that “transversely oriented shears,” i.e., the product of the EI<sub>s</sub> quantifying streamline crossing and averaged shear rate, indicated good mixing, as quantified by the decay of the variance of concentration. Each of these models “blinked” between two different flow patterns. McIlhany and Wiggins<sup>17</sup> considered a kinematic model of a spatially periodic channel flow that incorporated the separatrix map in a way that allowed for two or three distinct flow patterns for the cross-sectional flow in each spatial period. This resulted in a two dimensional mapping that “blinked” between two or three distinct flow patterns. The Eulerian indicator that quantified “streamline crossing” (henceforth, termed “transversality”) was generalized to deal with this new situation, where it was found that three distinct cross-sectional flows could produce optimal mixing in comparison to two distinct cross-sectional flows (where quality of mixing was measured by the decay of the variance of concentration). McIlhany *et al.*<sup>18</sup> further developed the notion of Eulerian indicators (EI<sub>s</sub>) for predicting Lagrangian mixing behavior in the context of considering a two dimensional duct flow that alternates between two distinct velocity fields that were calculated using a lid-driven cavity model, i.e., a two dimensional blinking flow. They introduced a new EI, termed “mobility,” that provides an Eulerian measure of how effectively the blinking velocity fields transport fluid throughout the domain. They showed that although individually the mobility and transversality did not correlate well with mixing as measured by the decay of the variance of concentration, the *product* of mobility and transversality does correlate well with the decay of the variance of concentration and predicts which combinations of velocity fields will produce the most effective mixing. McIlhany and Wiggins<sup>19</sup> extended the notion of EI<sub>s</sub> to the continuous time setting for two dimensional flows with arbitrary time dependence. In particular, they considered mixing in a kinematic model of a time dependent double-gyre with five different types of time dependencies—sinusoidal, sawtooth, square wave, triangular, and noise. Using the variance of concentration as a mixing diagnostic, they found that noisy time dependence had the largest region of good mixing in the parameter space and triangular time dependence had parameter values corresponding to the most complete and fastest mixing. These Lagrangian based predictions were confirmed by the EI<sub>s</sub> (product of the transversality and mobility). Although not every feature of the mixing behavior was captured by EI<sub>s</sub>, they showed that they do, in general, predict the regions in the parameter space that correspond to good mixing. Moreover, the EI<sub>s</sub> offered a factor of 100 computational advantage in exploring the parameter space in comparison with the trajectory based mixing diagnostic.

In this paper, we generalize the notion of EI<sub>s</sub> to three dimensional unsteady flows (which are not necessarily periodic in time). Most of the work on the dynamical systems approach to Lagrangian transport has been for two dimensional, time-periodic flows. Motivation for aperiodicity in time comes from geophysical fluid flow applications (see, e.g., Refs. 9, 20, and 21) and a relatively recent application that has motivated studies in three dimensions has been mixing at the microscale, see, e.g., Refs. 22–30. Early work discussing the dynamical systems approach to transport in three dimensions can be found in Refs. 31–33. In this paper, we consider mixing associated with the Hills spherical vortex (for background, see Ref. 34). The Hills spherical vortex is an excellent example for studying three dimensional transport phenomena since it allows the type of external time dependence to be explicitly chosen and controlled as well as the basic symmetry properties of the flow can be chosen with an appropriate choice of parameters (i.e., the axisymmetric case and the fully three dimensional cases can be compared and contrasted). In particular, the flow we consider is a three dimensional, time dependent analog of the oscillating vortex pair flow studied in Ref. 35, where the method of lobe dynamics<sup>36</sup> was first introduced in fluid mechanics.

This paper is outlined as follows. In Sec. II, we describe the flow generated by the Hills spherical vortex in a linear, time-dependent strain rate field. In particular, we focus on the geometrical properties of the flow, strain rate field, and the time dependence under consideration. In Sec. III, we describe how we characterize Lagrangian transport. This is particularly important since the flow is an open flow. The open flow nature of the flow is dealt with through the introduction of the *downstream separation distance* (DSD) and the *escape variance*. In Sec. IV, we develop the notion of EIs for three dimensional time dependent flows. Of particular note, the “transversality” for three dimensional flows is very different from the two dimensional notion, and in Sec. IV B, we spend some time motivating the differences and describing the algorithm for its computation. Three additional EIs are introduced in Secs. IV C (the transverse shear), IV D (the relative rate of change of the velocity field or the RROC), and IV E (the mobility). These three EIs are “natural” generalizations of the EIs for two dimensional flows. In Sec. V, we describe a “composite” EI constructed from the four that we have described earlier that we use to predict mixing and transport properties. In Sec. VI, we describe the results of the EI computation and the Lagrangian quantification of transport and mixing and in Sec. VII, we compare the Eulerian and Lagrangian results and assess the capability of the EIs to predict Lagrangian transport. The EIs yield results consistent with the dynamics of the Hill’s vortex flow characteristics, correlation with transverse shear, and anti-correlation with transversality. Finally, in the Appendices, we provide additional details on the computation of the EIs.

## II. HILL’S SPHERICAL VORTEX

In this section, we provide the necessary background on the velocity field due to Hill’s spherical vortex in a (linear) time-dependent strain rate field. Details and background can be found in Ref. 34. The velocity field,  $\mathbf{v}$ , that we will analyze, as shown in Fig. 1, has the general form,

$$\begin{aligned} \mathbf{v} &= H(x, y, z) + S(x, y, z, t), \\ H_x &= (u_r \sin \Theta + u_\Theta \cos \Theta) \cos \Phi, \\ H_y &= (u_r \sin \Theta + u_\Theta \cos \Theta) \sin \Phi, \\ H_z &= (u_r \cos \Theta - u_\Theta \sin \Theta), \\ u_r &= \begin{cases} U(1 - a^3/r^3) \cos \Theta, & \text{if } r \geq a, \\ -\frac{3}{2}U(1 - r^2/a^2) \cos \Theta, & \text{if } r < a, \end{cases} \\ u_\Theta &= \begin{cases} -U(1 + a^3/(2r^3)) \sin \Theta, & \text{if } r \geq a, \\ \frac{3}{2}U(1 - 2r^2/a^2) \sin \Theta, & \text{if } r < a, \end{cases} \end{aligned} \quad (1)$$

where  $[r, \Theta, \Phi]$  are the radius, polar, and azimuthal angles, respectively, and  $U = 1$  and  $a = 1$ .

If the vertical axis is the  $z$  axis, we see from this expression that the Hill’s spherical vortex velocity field,  $H(x, y, z)$ , is axisymmetric, i.e., it is unchanged with respect to rotation about the  $z$  axis. The matrix  $S$  of the linear strain rate field is given by

$$\begin{aligned} S &= \mathcal{A}(t)\delta^{-1} \begin{bmatrix} a(t) & 0 & 0 \\ 0 & \beta(t) & 0 \\ 0 & 0 & \gamma(t) \end{bmatrix} \delta \begin{bmatrix} x \\ y \\ z \end{bmatrix}, \\ \delta &= \begin{bmatrix} \cos \psi \cos \varphi - \sin \psi \cos \theta \sin \varphi & \cos \psi \sin \varphi + \sin \psi \cos \theta \cos \varphi & \sin \psi \sin \theta \\ -\sin \psi \cos \varphi - \cos \psi \cos \theta \sin \varphi & -\sin \psi \sin \varphi + \cos \psi \cos \theta \cos \varphi & \cos \psi \sin \theta \\ \sin \theta \sin \varphi & -\sin \theta \cos \varphi & \cos \theta \end{bmatrix}, \end{aligned} \quad (2)$$

where  $A(t)$  is some time dependent function.

Now we describe the specific cases that we want to consider. In particular,  $\theta$ ,  $\phi$ , and  $A(t)$  change depending on the case considered.

**Case 1: Steady, unperturbed (i.e.,  $S(x, y, z, t) = 0$ ):** This is just the velocity field due to Hill's spherical vortex. For  $S(x, y, z, t) = 0$ , the flow is steady and has hyperbolic stagnation points at

$$\begin{aligned} h_1 &= (0, 0, -a), \\ h_2 &= (0, 0, a), \end{aligned}$$

where  $h_1$  has a one dimensional stable manifold and a two dimensional unstable manifold, and  $h_2$  has a two dimensional stable manifold and a one dimensional unstable manifold.

**Case 2: Steady, non-axisymmetric perturbation:** In this case, the flow is still steady, but the flow is fully 3D and can be chaotic. The best choice for the strain rate field is not clear. Building on what has already been done in the earlier work<sup>37</sup> and extended in this study, we used the following parameters:

$$\begin{aligned} \mathcal{A}(t) &= \mathcal{A} = 0.3, \\ \theta &= 0.5, \quad \varphi = 5, \quad \psi = 0, \\ \alpha(t) &= -0.5, \quad \beta(t) = -0.5, \quad \gamma(t) = 1. \end{aligned}$$

**Case 3: Unsteady, non-axisymmetric perturbation:** This is the general case treated in Refs. 37 and 38, compared to which we have adjusted the amplitude parameter  $A(t)$  to remove the Gaussian envelope, and  $\theta$  to be a (range of) constant azimuthal angle that does not vary with time,

$$\begin{aligned} \mathcal{A}(t) &= 0.3 + 0.27 \sin(3.3t), \\ \theta &= \theta_{\text{tilt}}, \quad \varphi = 5t, \quad \psi = 0, \\ \alpha(t) &= -0.5, \quad \beta(t) = -0.5, \quad \gamma(t) = 1. \end{aligned}$$

The linear strain fields' axis was varied away from the polar axis,  $\theta_{\text{tilt}}$ , over the range  $[0, 90^\circ]$ .

## A. Domains, ranges, and averages

The Eulerian calculations performed for this study limit the domain to a rectangular box with sides extending to  $\pm 1.2$ , while the Lagrangian simulations slightly extend this domain to an X-Y plane limited to  $\pm 1.2$ , while the Z-domain extends from  $-1.2 \leq z \leq +2.0$ . The reason for this choice of domain is that the perturbed model used in this study allows for fluid particles to leave the unit sphere as well as entrain particles from outside the spheres' boundary. As shown in Ref. 37, interesting lobe dynamics occur at locations near the surface and along the downstream flow in a plume depending on the size of the perturbation. By considering a slightly larger domain than the unit sphere, the EIs may capture some of the Lagrangian aspects of this flow. Care must be taken not to extend the domain too far beyond the unit sphere as the unperturbed vortex is defined as two flows, an exterior flow which moves outside of the unit sphere and a separated re-circulating flow within. By adding a linear strain field as a time varying perturbation, the perturbed flow extends beyond the unit sphere and grows with distance. Without a mechanism to curtail the strain field, as particles move away from the origin, they are dominated by the strain field, falling outside the interest of this study.

Before the formulas which define the Lagrangian and Eulerian metrics are given, we begin by establishing some general notation. The flow will be defined on a general three dimensional domain, denoted  $\mathcal{D}$ . For the Hill's vortex model that we consider,

$$\mathcal{D} = \{(x, y, z) \in \mathbb{R}^3 \mid -1.2 \leq x \leq 1.2, -1.2 \leq y \leq 1.2, -1.2 \leq z \leq 2.0\}. \quad (3)$$

The flow will depend on one parameter, and we will denote the space of this parameter by  $\mathcal{P}$ , and a particular point in this parameter space by  $\mu$ . For the Hill's vortex model,

$$\mathcal{P} = \{(\theta_{\text{tilt}}) \in \mathbb{R}^1 \mid 0 \leq \theta_{\text{tilt}} \leq 90^\circ\}. \quad (4)$$

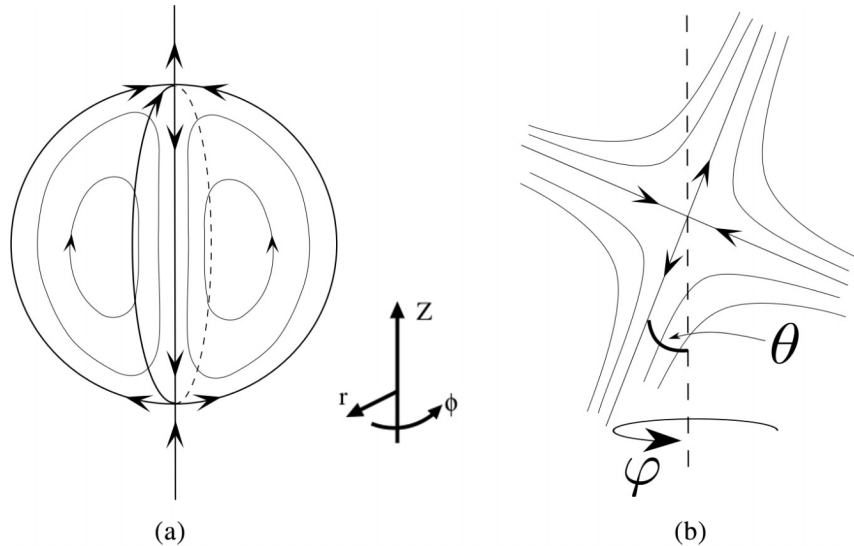


FIG. 1. Illustration of the flow for the undisturbed Hill's vortex (a) as well as the linear strain field applied as a time-varying perturbation (b).

The flow will be time dependent and defined over a time interval denoted  $\mathcal{I} \equiv [0, t_f]$ , where  $t_f = 25$  in non-dimensional time units. The velocity field is denoted by

$$\begin{aligned}\dot{x} &= v_x(x, y, z, t; \mu), \\ \dot{y} &= v_y(x, y, z, t; \mu), \quad (x, y, z) \in \mathcal{D}, t \in \mathcal{I}, \mu \in \mathcal{P}, \\ \dot{z} &= v_z(x, y, z, t; \mu),\end{aligned}$$

or, in vector form

$$\dot{\mathbf{r}} = \mathbf{v}(\mathbf{r}, t; \mu), \quad (5)$$

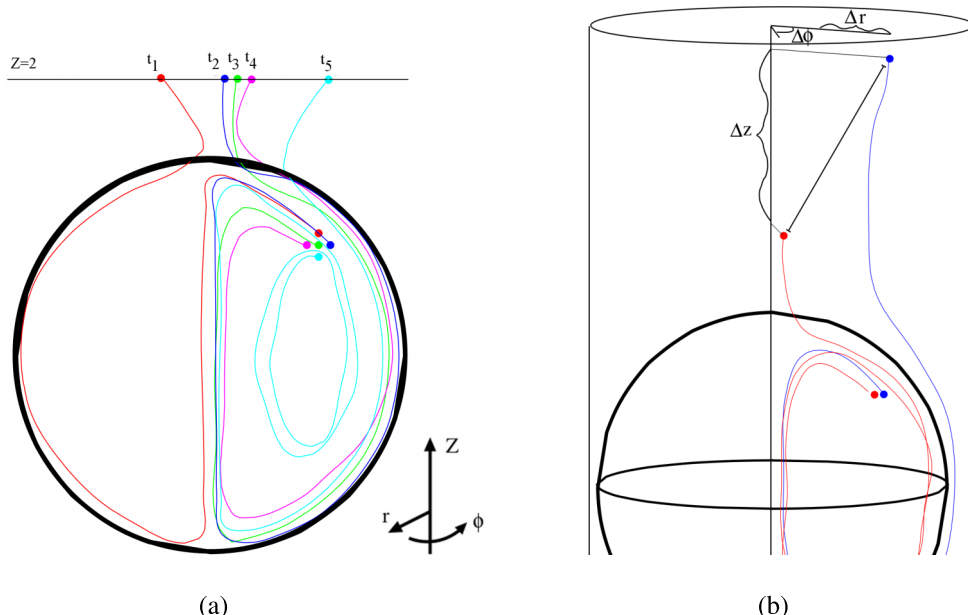


FIG. 2. Escape times and DSD illustrations. (a) Sampling of escape times around a neighborhood. (b) DSD.

where  $\mathbf{r} \equiv (x, y)$ ,  $\mathbf{v}(\mathbf{r}, t; \mu) \equiv (v_x(x, y, z, t; \mu), v_y(x, y, z, t; \mu), v_z(x, y, z, t; \mu))$ . We will need to perform averages of certain functions over the flow domain and the time interval. For a general function  $\mathbf{v}(\mathbf{r}, t; \mu)$ , these averages are denoted by

$$\langle \mathbf{v}(\mathbf{r}, t; \mu) \rangle_{\mathbf{r}} \equiv \frac{1}{\int_{\mathcal{D}} d\mathbf{r}} \int_{\mathcal{D}} \mathbf{v}(\mathbf{r}, t; \mu) d\mathbf{r}, \quad (6)$$

$$\langle \mathbf{v}(\mathbf{r}, t; \mu) \rangle_t \equiv \frac{1}{t_f} \int_0^{t_f} \mathbf{v}(\mathbf{r}, t; \mu) dt. \quad (7)$$

### III. LAGRANGIAN QUANTIFICATION OF TRANSPORT

Our Lagrangian approach to quantify the transport properties of the vortex looked to capture the behavior of particles near the center of the vortex. Except in case one, the velocity field in the far field  $R \gg 1$  is dominated by the linear strain field, and distance traveled as a function of time is exponential. We are interested primarily in the transport effects of the vortex, so we created a metric defined below, the DSD, to measure the spread in particle position caused by the vortex without considering the far field behavior.

First, we consider a cylindrical domain ranging from  $0 < \theta < 90^\circ$ ,  $0 < r < 1.2$ , and  $-1.2 < z < 1.2$ . We populated the domain with particles spaced on regular 2D Cartesian grids with  $\Delta r = 0.01$ , and  $\Delta z = 0.01$  placed at some angle  $\theta$  to the x-axis. We created several such slices to approximately cover the domain cylindrically with  $\Delta\theta = 10^\circ$  (0.17 rad), and for each such slice, we added two more grids displaced along the transverse direction by  $\Delta r_{\text{transverse}} = 0.01$ . We chose an approximately cylindrical grid to take advantage of the approximate cylindrical symmetry of the vortex to reduce computational costs, and we added adjacent “wing” grids so as to have nearest neighbors along three perpendicular axes.

We then evolved all the particles according to the perturbed Hill’s spherical vortex velocity fields until one of the following two conditions was met:

1. The particle escaped the sphere. Due to the nature of the velocity field, once the particle has crossed some boundary along the z axis, it can never return to the vortex. We used  $z_{\text{cut}} = 2.0$  as an appropriate value—large enough to be sure to have escaped perturbations of the vortex, but small enough that the exponential nature of the linear strain field does not dominate.
2. Time  $t = t_{\max}$  was reached. This case would occur for particles that either never escaped the sphere, or would do so on a long enough time scale that dynamically they represent trapped regions. We chose  $t_{\max} = 25$ .

When either condition was met, we recorded the time  $t_{\text{esc}}$ , and the position  $r_{\text{esc}}, \theta_{\text{esc}}$ , equivalent to  $x_{\text{esc}}, y_{\text{esc}}$  in Cartesian coordinates. This method defines an escape time and transverse escape position for every point sampled in our domain. Between any two neighboring points, we define a DSD in this manner,

$$DSD(r, s; \mu) \equiv \sqrt{c^2(t_{\text{esc}}^r - t_{\text{esc}}^s)^2 + (x_{\text{esc}}^r - x_{\text{esc}}^s)^2 + (y_{\text{esc}}^r - y_{\text{esc}}^s)^2}, \quad (8)$$

where the assumption is made that once particles have passed the threshold plane at ( $z_{\text{cut}} = 2.0$ ), the particles continue downstream at a constant speed denoted as “c.” The DSD represents the Euclidean separation distance between two particles initially near each other on the grid based on the escape time of each particle, shown in Fig. 2.

A point of note is the appearance of  $c\Delta t_{\text{esc}}$  instead of  $\Delta z_{\text{esc}}$ . In the near exterior region,  $1 < R < 2$ , the particle speed  $c$  is approximately 1. Neglecting the contribution of the linear strain field (appropriate, if  $z_{\text{cut}}$  is not large), we say that the difference in time,  $\Delta t_{\text{esc}}$ , is directly proportional to the difference in distance parallel to the z axis,  $\Delta z$ , that the particles travel over the time interval, with  $c = 1$ . In other words, we assume that far from the vortex particles travel with a plug flow profile, and we explicitly stop calculations at  $z = z_{\text{cut}}$  so that the linear strain field does not disturb that assumption. Additionally, we calculated an Upstream Separation Distance,  $USD(r, s; \mu)$ , calculated from  $t_{\text{ent}}$ ,  $r_{\text{ent}}$ , and  $\theta_{\text{ent}}$  by integrating time backwards from 0 to  $-t_{\max}$ . This quantity

measures how far apart currently neighboring particles were before they entered the vortex, and captured the possibility that the vortex might bring initially distant particles together at the time  $t = 0$ .

At each point, we determine the local escape variance ( $\mathcal{V}$ ) using the DSD and USD of the point  $r$  and its neighbors with the formula

$$\mathcal{V}(r; \mu) \equiv \frac{1}{N} \sum_{s \in N(r)} DSD(r, s; \mu)^2 + USD(r, s; \mu)^2. \quad (9)$$

We call this quantity  $\mathcal{V}$  the Escape Variance because it is constructed by analogy to a typical variance, where  $DSD(r, s)^2$  has taken the role of  $(x(r) - x(s))^2$ , that is, it is a variance off of the center, not off of the mean. This quantity represents the spread of the downstream particles positions, which were initially in the neighborhood of the particle located at position  $r$ .

In regions where nearby particles escape together, their DSD is small; these regions occur both inside and outside the vortex. In regions that never escape,  $t_{esc}$  is defined to be  $t_{max}$ , and both  $r_{esc}$  and  $\theta_{esc}$  are defined to be whatever values they take at  $t = t_{max}$ . In all three cases, the  $\Delta t_{esc}$ ,  $\Delta r_{esc}$ , and  $\Delta\theta_{esc}$  between neighboring particles will be small, and the escape variance will also be small in such regions. Conversely, in regions of high stretching and folding, nearby particles may escape the vortex at very different times and positions. Correspondingly,  $\Delta t_{esc}$ ,  $\Delta r_{esc}$ , and  $\Delta\theta_{esc}$  will be large, so the escape variance will be large as well.

Once we have calculated the escape variance, we apply a thresholding function to determine what fraction of the domain has high escape variance values. For this calculation, we choose the domain to be  $R < 1$  for normalization purposes only; outside the vortex,  $\mathcal{V} < \mathcal{V}_{thresh}$  for all reasonable values of  $\mathcal{V}_{thresh}$ . Our final value, normalized to the size of the domain, is taken to be

$$\mathcal{I}(\mathbf{r}; \mu) \equiv \begin{cases} 0 & \mathcal{V}(\mathbf{r}; \mu) \leq \mathcal{V}_{thresh}, \\ 1 & \mathcal{V}(\mathbf{r}; \mu) > \mathcal{V}_{thresh}, \end{cases} \quad (10)$$

$$\Upsilon(\mu) \equiv \langle \mathcal{I}(\mathbf{r}, t; \mu) \rangle_{\mathbf{r}} \equiv \frac{1}{\int_{\mathcal{D}} d\mathbf{r}} \int_{\mathcal{D}} \mathcal{I}(\mathbf{r}; \mu) d\mathbf{r}. \quad (11)$$

This value,  $\Upsilon$ , is the fraction of the domain for which the local escape variance exceeds some threshold, and we will henceforth drop the arguments.

#### IV. EULERIAN CHARACTERIZATION OF FLOW

EIs have proven useful in the previous studies at highlighting features in a flow which promote mixing.<sup>16–19</sup> EIs are metrics based solely on information from the velocity field and its time dependence. Properties such as transversality, transverse shear, and the relative rate of change, as well as the amount of transport, are given quantitative values which when put together indicate regions in the flow which may promote mixing and transport. By considering configurations of micro-mixers which have a higher portion of the domain which promotes mixing, designs of micro-mixers were identified as optimized mixers relative to other configurations. For the case of the Hill's vortex with a time-varying perturbation, the choice of tilt-angle for the linear strain field is used as the parameter to adjust for optimization. As discussed in Sec. III, “mixing” is not the proper description of flows near a Hill's vortex, rather, the escape variance of the DSD and USD is considered as a metric to compare to EIs in order to characterize the flow.

##### A. Eulerian indicators in three dimensions—definitions

Applying EIs to the Hill's vortex requires the calculations to be performed in three dimensions, requiring a revision of previous definitions to be re-written for three dimensions. In all of the metrics considered, all definitions were easily translated into 3D with the exception of transversality ( $\alpha$ ), which required special care in its redefinition. Transversality ( $\alpha$ ) will be discussed first,

followed by transverse shear ( $\beta$ ), followed by the RROC, and then transport will be addressed by discussing mobility ( $\eta$ ).

The challenge in re-defining the EIs for three dimensions is in maintaining the previous definitions found in the papers.<sup>16–19</sup> In the process of re-defining the EIs for three dimensions, it was realized that each new definition ( $\beta$ , RROC,  $\eta$ ) was extendable into higher dimensions by a simple extension from  $N = 3$  to simply  $N$ . Transversality proved to be difficult to translate into  $N$ -dimensions; however, a definition was found which allows for a fully  $N$ -dimensional definition of transversality ( $\alpha_N$ ) and is given in Appendix A. The definition for three dimensions is given in Sec. IV B, utilizing the  $N$ -dimensional approach, simply reduced to  $N = 3$ .

## B. Transversality in three dimensions— $\alpha_{3D}$

The idea of transversality is to measure the amount of transverse components a set of vectors have relative to their longitudinal components. Initially, in two dimensions, and considering flows for blinking maps, transversality was a simple calculation of the angle between a velocity vector at a fixed location in the domain for two different times.<sup>16–18</sup> This concept was later extended to include continuous time-varying velocity vector fields by changing the definition to act as a measure of the spread of the set of angles formed by including all velocity vectors at a fixed point in the domain over a time window in which the velocity vector is allowed to change continuously.<sup>19</sup> In each of these papers, the flow was two dimensional, such that the angle defined was either an angle between two vectors or a polar angle around the mean vector of a set. When considering a continuous time-varying velocity field in three dimensions, more than one angle is needed to describe the relationship between a set of vectors with respect to a mean vector. This requires the definition of transversality ( $\alpha$ ) to change once more from its previous definitions.

The following prescription is given to calculate the transversality in three dimensions. Consider the set of velocity vectors at some fixed position,  $\mathbf{r}$  over some interval of time,  $[0, t_f]$ . The transversality measures the angular spread of these vectors over time with respect to how transverse the vectors are to the mean vector of the set. There are two components to measuring the transversality in 3D. The first is the transversality of angles with respect to the polar axis, dubbed  $\alpha_{\theta 3}$ . The second component measures the spread of the angles of the vectors as projected onto the great circle of the unit sphere, in other words, the azimuthal spread, dubbed  $\alpha_{\theta 2}$ . The final value calculated for the 3D transversality is a linear combination of the two values,  $\alpha_{\theta 3}$  and  $\alpha_{\theta 2}$ , where the coefficients of the terms are based on the dimension fullness,  $D_3$ , parameter and two normalizing cases given in Appendix B.

### 1. Singular value decomposition (SVD)

The first step in calculating the transversality is to measure the fullness of the dimensions spanned by the vector set. SVD when applied to a set of vectors assumes the tails of all vectors are at the origin, making the data points used by SVD the tips of the vectors. SVD calculates a scaling matrix as well as two rotation matrices, giving the sense of the ellipsoid formed by the set of vectors. The scaling matrix diagonal components given by the values  $(a, b, c)$  represent the dimension scales, where  $a$  is the largest component,  $b$  is the middle scaled value, and  $c$  is the smallest scale. The left-hand rotation matrix derived from SVD,  $U$ , can be used to rotate the coordinate system such that the vector set is re-aligned from its initial orientation  $(x, y, z)$  to a new set of axes  $(x', y', z')$  where  $z'$  points along the longest scale axis defined by the vector sets mean. The new axis  $x'$  points along the second largest scale axis and  $y'$  points along the smallest scale axis. The fullness of the dimension that the vector set spans is defined as the relative size of  $a$  to  $b$  and  $c$ ,

$$D_3 = \frac{c^2}{a \times b}, \quad (12)$$

where  $a$ ,  $b$ , and  $c$  are the three scaling parameters given by the SVD, equivalent to the semi-major and semi-minor axes for a  $N$ -dimensional ellipsoid with  $a \geq b \geq c$ . The first ratio,  $\frac{c}{b}$ , gives the oblateness value between the two lower dimensions and the second ratio,  $\frac{c}{a}$ , properly gives the scale

factor that is needed to measure how collapsed the vector set is in a lower dimension. The dimension parameter should give a low value (near zero) when the distribution of vectors only spans a two dimensional space, but should give a high value (near one) when the vector set fully spans three dimensions. It is worth noting that the dimension parameter,  $D_N$ , is itself an EI determining the fullness of a set of velocity vectors.

Once the SVD has been calculated on the vector set, the newly oriented vectors have—by definition—a mean velocity vector pointing along the  $z'$  axis. Calculating the polar angle,  $\theta_3$  is straightforward. Calculating the azimuthal angle will also be necessary but will be treated as a polar angle in two dimensions, which will be called  $\theta_2$  for consistency with the general definitions given in Appendix C,

$$\tilde{\theta}_3 = \cos^{-1} \left( \frac{\|v'_z\|}{\sqrt{v'^2_x + v'^2_y + v'^2_z}} \right), \quad (13)$$

$$\tilde{\theta}_2 = \cos^{-1} \left( \frac{\|v'_x\|}{\sqrt{v'^2_x + v'^2_y}} \right), \quad (14)$$

where the absolute values of  $x'$  and  $z'$  have been used in order to fold the polar angles to be less than  $90^\circ$ .

## 2. Calculation steps of $\alpha_{3D}$

The following steps are taken to calculate the 3D transversality. The operations  $\hat{\mathcal{F}}_1$  and  $\hat{\mathcal{F}}_2$  are folding operations about  $90^\circ$  and  $45^\circ$ , respectively.

1. For a fixed location in the domain,  $\mathbf{r}$ , consider the set of velocity vectors over a time range from  $[0, t_f]$ .
2. Normalize the vector set such that the vectors all lie on a unit sphere.
3. Calculate the SVD of the vector set.
4. Rotate the vector set by the rotation matrix obtained from SVD to obtain a new set of vectors,  $\mathbf{v}' = U^\top \mathbf{v}$ , whose components are given by  $v'_x$ ,  $v'_y$ , and  $v'_z$ .
5. From the scaling matrix obtained from SVD, compute the dimension fullness parameter,  

$$D_3 = \frac{c^2}{a \times b}.$$
6. Calculate the polar angle transversality,  $\alpha_{\theta 3}$ , as follows.
  - Define the polar angle for the three dimensions,  $\theta_3$ .
  - Fold the polar angles to be less than  $90^\circ$ :  $\tilde{\theta}_3 = \hat{\mathcal{F}}_1[\theta_3]$ .
  - Calculate the variance of the folded angle:  $\mathcal{V}(\tilde{\theta}_3) = \frac{1}{N} \sum_{i=1}^N (\tilde{\theta}_3 - 0^\circ)^2$ .
  - Calculate the standard deviation of the variance:  $\sigma(\tilde{\theta}_3) = \sqrt{\mathcal{V}(\tilde{\theta}_3)}$ .
  - Fold the rms value about  $45^\circ$  and normalize to  $90^\circ$  to obtain the polar transversality:  $\alpha_{\theta 3} = 2\hat{\mathcal{F}}_2[\sigma(\tilde{\theta}_3)]$ .
  - The whole calculation can be summarized in one formula:  $\alpha_{\theta 3} = 2\hat{\mathcal{F}}_2 \left[ \sqrt{\frac{1}{N} \sum_{i=1}^N (\hat{\mathcal{F}}_1[\theta_3] - 0^\circ)^2} \right]$ .
7. From the rotated set of vectors,  $[v'_x, v'_y, v'_z]$ , create subsets of vectors by removing the  $z'$  coordinate, creating a set of  $N$  vectors spanning the two dimensional space  $(x', y')$ .
8. Calculate the polar angle transversality,  $\alpha_{\theta 2} = 2\hat{\mathcal{F}}_2 \left[ \sqrt{\frac{1}{N} \sum_{i=1}^N (\hat{\mathcal{F}}_1[\theta_2] - 0^\circ)^2} \right]$ .
9. Calculate the 3D transversality by taking the linear combination of the two values,  $\alpha_{\theta 2}$  and  $\alpha_{\theta 3}$ ,

$$\alpha_{3D} = (1 - 2D_3)\alpha_{\theta 3} + 2D_3\alpha_{\theta 2}, \quad (15)$$

where the coefficients for the linear terms of the two alphas come from normalizing to two special cases, discussed further in Appendix C.

### C. Transverse shear

The transverse shear, denoted as  $\beta$ , measures how much a fluid packet experiences a shear in the perpendicular direction relative to the flow's overall direction. Figure 3 illustrates how this shearing can occur. When a location in a flow has high transverse shear, fluid particles tend to drift away from their current trajectories onto new ones. At a given point in the velocity field, the gradient of the magnitude of that velocity vector (shown as  $\rho$ ) is projected onto the velocity vector. From this, the transverse component is easily found, dubbed  $\beta$ .

Although an obvious change would be to redefine  $\beta$  as the magnitude of the cross product of  $\rho$  and  $v$ , the best reason to keep the definition as it is presented in Eq. (18) is that these definitions are trivially extendable to higher dimensions,

$$\rho(\mathbf{r}, t; \mu) = \vec{\nabla}|\mathbf{v}(\mathbf{r}, t; \mu)|, \quad (16)$$

$$\rho(\mathbf{r}, t; \mu) \cdot \hat{\mathbf{v}} = |\rho(\mathbf{r}, t; \mu)| \cos(\phi), \quad (17)$$

$$\beta(\mathbf{r}, t; \mu) = |\rho(\mathbf{r}, t; \mu)| \sin(\phi), \quad (18)$$

where  $\phi$  is the angle between  $\rho$  and  $\hat{\mathbf{v}}$ .

Transverse shear differs from the other EIIs in that it solely depends on its spatial structure, i.e., it is time independent. All other EIIs in this study depend on a collection of velocity vectors over time. In the case of transversality, the collection serves to define both the mean and the spread of the distribution. The RROC requires several points in a time-series of velocity vectors to define an average rate of change and the mobility is an integral over time.

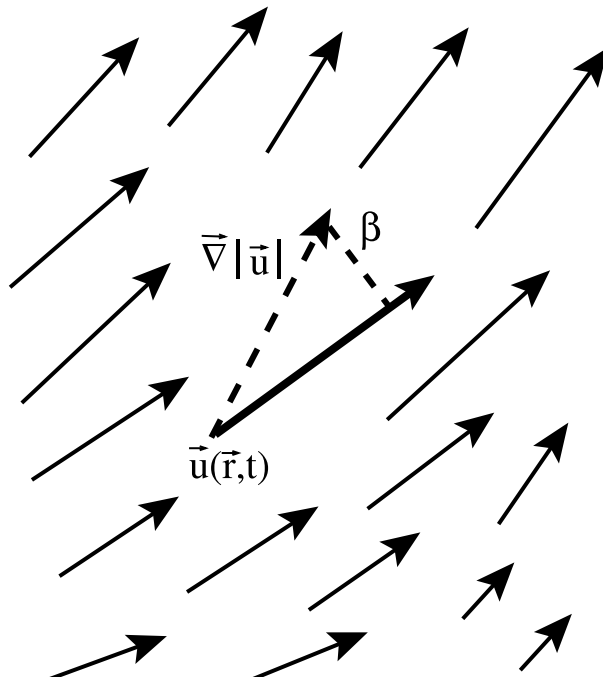


FIG. 3. A velocity vector field with a spatial gradient, depicting the gradient to the field at a point. The gradient vector,  $\rho$ , is along the acceleration. The transverse shear,  $\beta$ , is the transverse component of  $\rho$  with respect to the velocity vector,  $v$ .

## D. RROC

The *RROC* has been defined previously,<sup>19</sup> so a short summary of its properties is given in this section. The *RROC* measures a scale independent rate of change of a velocity vector over time. The *RROC* is sensitive to both changes in magnitude as well as direction, with instantaneous values peaking at a maximum of 1.0 whenever the velocity changes sign (in 1D) or rotates by 180° in one time step. The *RROC* integrates the differential change,  $\Delta w(\mathbf{r}, t; \mu)$ , which is bounded over the interval [0, 1] and defined next. The differential change is integrated over a time window given by the interval [0,  $t_f$ ], and then divided by that length time, yielding a rate. The *RROC* is interpreted as the rate of change the velocity field undergoes to be used in contrast to the rate of change that particles in the fluid experience. When the value for the *RROC* is low, the velocity field is near or at steady flow. When the value is high, the velocity field is changing rapidly, possibly due to turbulence or when a location in the field is near a moving stagnation point,

$$\Delta w(\mathbf{r}, t; \mu) = \frac{\| \mathbf{v}(\mathbf{r}, t + \Delta t; \mu) - \mathbf{v}(\mathbf{r}, t; \mu) \|}{\| \mathbf{v}(\mathbf{r}, t + \Delta t; \mu) \| + \| \mathbf{v}(\mathbf{r}, t; \mu) \|} = \begin{cases} 0 & \text{if } \mathbf{v}(\mathbf{r}, t + \Delta t; \mu) = \mathbf{v}(\mathbf{r}, t; \mu) \\ 1 & \text{if } \mathbf{v}(\mathbf{r}, t + \Delta t; \mu) = -\mathbf{v}(\mathbf{r}, t; \mu) \\ 1 & \text{if } \mathbf{v}(\mathbf{r}, t + \Delta t; \mu) = 0 \\ 1 & \text{if } \mathbf{v}(\mathbf{r}, t; \mu) = 0 \end{cases}, \quad (19)$$

$$dw(\mathbf{r}, t; \mu) = \lim_{\Delta t \rightarrow 0} \Delta w(\mathbf{r}, t, \Delta t; \mu), \quad (20)$$

$$\frac{\partial w(\mathbf{r}, t; \mu)}{\partial t} = \lim_{\Delta t \rightarrow 0} \frac{\Delta w(\mathbf{r}, t, \Delta t; \mu)}{\Delta t}, \quad (21)$$

$$RROC(\mathbf{r}; \mu) = \tilde{w}(\mathbf{r}; \mu) = \frac{1}{t_f} \int_0^{t_f} \frac{\partial w(\mathbf{r}, t; \mu)}{\partial t} dt. \quad (22)$$

## E. Mobility

The EI for transport dubbed mobility,  $\eta(\mathbf{r}, t)$ , measures the consistency of the velocity field to transport particles away from the location under consideration. Defined initially in a previous study,<sup>19</sup> three basic components are required for this calculation, the *RROC*, a characteristic time,  $T_c$ , and the velocity integrals  $v_{fast}$  and  $v_{slow}$ . The *RROC* is defined in Sec. IV D. The characteristic time can be defined in a number of ways depending on the nature of the flow considered. For the Hill's vortex model in this study, a characteristic time,  $T_c = 3.3$ , was used as this is the average recirculation time for particles of fluid in the unperturbed vortex case. The main purpose of the characteristic time is to give meaning to the rate found by the *RROC*. The combination of the two values then properly weights the velocity integrals used in calculating the mobility.

The calculations for the velocity integrals are given below. When a flow is changing its direction quickly compared to the rate of passage of fluid particles, the velocity vectors are integrated first, then the magnitude for the total is dubbed  $v_{fast}$ . When a flow changes direction too quickly, the net displacement from a position in the domain is small as the integral of the vector leads to a smaller overall displacement. When a velocity field is slowly changing its direction, or is steady, compared to the rate of passage of fluid particles, the overall displacement away from the location in the domain should be higher as the velocity vector is consistently pushing the fluid away from its position. In this case, the magnitude is taken first for the velocity vector and then integrated and dubbed  $v_{slow}$ ,

$$v_{fast}(\mathbf{r}; \mu) \equiv \left| \int_0^{t_f} \mathbf{v}(\mathbf{r}, t; \mu) dt \right|, \quad (23)$$

$$v_{slow}(\mathbf{r}; \mu) \equiv \int_0^{t_f} |\mathbf{v}(\mathbf{r}, t; \mu)| dt. \quad (24)$$

The definition of “fast” and “slow” depends upon the time scale under consideration, and they are given meaning through the characteristic time scale,  $T_c$ , and the RROC, as follows:

$$\eta'(\mathbf{r}, t; \mu) \equiv v_{\text{sum}}(\mathbf{r}; \mu) \equiv (1 - e^{-\tilde{w}(\mathbf{r}; \mu)T_c}) v_{\text{fast}}(\mathbf{r}; \mu) + (e^{-\tilde{w}(\mathbf{r}; \mu)T_c}) v_{\text{slow}}(\mathbf{r}; \mu). \quad (25)$$

The mobility indicates the strength of transport away from its location in the domain. Stagnation points should have zero mobility, as should boundary locations where the flow approaches zero. Turbulent regions should also indicate frustrated transport over the time window of integration. Steady flow regions should indicate high transport, unless the magnitude of the flow is low. As transport is necessary for any kind of effect in the flow to be possible, the EI for transport, mobility, is used as a product to the other EIs. Transversality and transverse shear are additive as they represent two different properties of the flow, each to be enhanced by transport.

## V. COMPOSITE EULERIAN INDICATOR—OMEGA

The final form taken to summarize the effects calculated from the velocity field is dubbed Omega,  $\Omega$  and is given by the product of mobility times the sum of transversality and transverse shear,

$$\Omega(\mathbf{r}, t; \mu) = \eta'(\mathbf{r}, t; \mu) [\alpha_{3D}(\mathbf{r}, t; \mu) + \beta(\mathbf{r}, t; \mu)], \quad (26)$$

$$\langle \Omega(\mathbf{r}, t; \mu) \rangle_{\mathbf{r}} \equiv \frac{1}{\int_{\mathcal{D}} d\mathbf{r}} \int_{\mathcal{D}} \Omega(\mathbf{r}, t; \mu) d\mathbf{r}. \quad (27)$$

This form for the composite EI,  $\Omega$ , was chosen in keeping with the rationale provided previously in Ref. 19, where the mobility is explained to have the effect of enhancing any existing Eulerian qualities that promote mixing. As such, transversality and transverse shear are viewed as independent features of the velocity field, promoting displacement from stable orbits both temporally and spatially. In this sense, mobility enhances these two existing properties of the velocity field, but cannot by itself explain effects such as mixing. The definition of  $\Omega$  is an attempt at combining all of the EI sector into one value; however, there are reasons why this may not be desirable, which will be discussed in Secs. VI and VII. As such,  $\Omega$  may be useful as a reference value to compare to other metrics or simply to track changes in the status of the flow versus some parameter.

## VI. RESULTS: LAGRANGIAN AND EULERIAN

Presented next are the results of the Lagrangian metric for DSD as a function of the linear strain fields’ tilt angle,  $\theta_{\text{tilt}}$ . The EI results come next, also computed as a function of the tilt angle. The Lagrangian simulation of the flow was performed on a High Performance Computer (HPC) cluster utilizing 120 nodes running at 2.0 GHz and lasted for 45 days, giving a single node computational cost of  $9.3312 \times 10^{17}$  CPU cycles. The calculation was performed for a set of fluid particles initially on a grid  $240 \times 240$  for three planes over 32 azimuthal angles and then run over 50 different strain field angles. The simulations used a fourth order Runge-Kutta run on Matlab with an adaptive step size and an initial time step of 0.1 time units run until the time reached 25 units. The EIs were calculated over the same grid on field points, finishing on a single desktop computer running at 3 GHz in 2 h, for a computational cost of  $3.24 \times 10^{13}$  CPU cycles. The EIs were calculated 97 500 times faster than their Lagrangian counterparts.

### A. Lagrangian results

Our Lagrangian analysis of transport looked to examine behavior both in the spatial domain, and in the parameter domain as a function of  $\theta_{\text{tilt}}$ . In the spatial domain, separation along the z-axis was the dominant contribution to  $\mathcal{V}$ , showing the domain divided into four regions.

**Exterior unmixed flow:** Outside the vortex, the flow was smooth and nearby particles never separated. These particles mostly ignored the vortex, and  $\mathcal{V}$  is low.

**Interior unmixed flow:** Inside the vortex, there were large tongues that exited the vortex together.

Despite being captured by the vortex,  $\mathcal{V}$  is low because within each tongue particles are not separated from their neighbors. In general, these regions exited the sphere at earlier times, such that the effect from the interior dynamics—mainly shear—was minimized, keeping the regions together.

**Interior mixed flow:** The vortex also produced regions of stretching and folding as it sent particles around the equatorial stagnation point. Nearby particles experience large  $\Delta t_{esc}$  because their cycling times through the vortex vary greatly and they can exit the vortex at different spatial positions. These regions have the highest values of  $\mathcal{V}$ .

**Interior trapped flow:** Near the stagnation ring of the unperturbed Hills spherical vortex, there exists a region of particles that never escaped the vortex before  $t_{max}$ . These particles were trapped in the vortex for longer than the simulation length. While eventually they may escape with very large relative  $\Delta t_{esc}$ , they represent regions of low transport. Because  $t_{esc} = t_{max}$  identically in these regions,  $\mathcal{V}$  is low.

Figures 4(a)–4(d) show the results of the DSD and USD times only, where any differences in  $(r, \phi)$  are ignored. The panels are, respectively, DSD time for a cross-sectional plane at  $Z = 0$ —Fig. 4(a), the USD time for the XZ plane—Fig. 4(b), the DSD time for the XZ plane—Fig. 4(c), and the combined DSD-USD time for the XZ plane—4(d). The  $Z = 0$  plane shows the effect of the precession of the linear strain field in the escape times.

When we looked at the USD, we found the same classification of regions distributed differently in space—approximately flipped across the plane  $z = 0$ . Together, the quantity  $t_{esc} - t_{ent}$  more finely partitioned the domain into checkerboard regions of interior unmixed flow and interior mixed flow consistent with lobe dynamics occurring near the boundary of the unit sphere.<sup>39</sup>

In order to quantify those subdomains that remain together after some time has passed, the variance of each location is considered and shown in Fig. 5. In this figure, at each tilt angle chosen (34 evenly spaced angles from  $0^\circ$ - $90^\circ$  plus 18 more near  $48^\circ$  for refinement), the DSD variance for time is spatially averaged over a cylindrical domain with a radius of 1.2 and ranging from  $-1.2 < Z < 1.2$ . In the figure, at each location in the domain, the variance is compared to a threshold value and then counted. The value,  $\Upsilon$ , described earlier is the percentage of the domain greater than the threshold value. In the figure, three threshold values are shown: 0.04 represents a final separation of 0.2 which is relatively close together, a second threshold of 1.0 represents a final separation of the radius of the sphere, and the final threshold of 4.0 represents a final separation of the spheres' diameter, which represents a large degree of separation for neighboring fluid particles. The lowest contour in the figure shows the DSD positional variance, which shows that at  $\theta_{tilt} = 48^\circ$ , the precession of the linear strain field has the largest effect to force particles out of plane. The unperturbed Hill's vortex does not allow particles to change azimuthal planes.

In the parameter domain, we examined  $\Upsilon$  as function of the angle  $\theta_{tilt}$  and found three main trends.

First,  $\Upsilon$  was the highest for  $\theta_{tilt} = 0^\circ$  and the lowest for  $\theta_{tilt} = 90^\circ$ , and with an overall downward trend as  $\theta_{tilt}$  increased. Particularly, this means that transport, as quantified by the DSD, was the greatest in the axisymmetric case. We believe this overall trend relates to the surface area of the vortex as follows. When  $\theta_{tilt} = 0^\circ$ , in the equatorial band, the linear strain field has consistent eigenvalues with the same sign ( $\alpha = \beta = -0.5$ ). This means that the entire tropical area is engaged in moving particles in and out of the vortex, and represented visually in Figs. 6(a) and 6(b).

In contrast, when  $\theta_{tilt} = 90^\circ$ , the equatorial band has eigenvalues of opposite sign ( $\gamma = 1$  and  $\beta = -0.5$ ), which means that between the major axes exist regions where the linear strain field is approximately tangent to the surface of the sphere. In these regions, transport across the surface of the sphere is inhibited.

The second major trend we found was the local maximum in  $\Upsilon$  near  $\theta_{tilt} = 50^\circ$ . This corresponds to a maximally unsymmetric linear strain field, none of whose principal axes align with the axis of symmetry of the unperturbed Hills spherical vortex. In this case, the  $\Delta x_{esc}^2 + \Delta y_{esc}^2$  term in

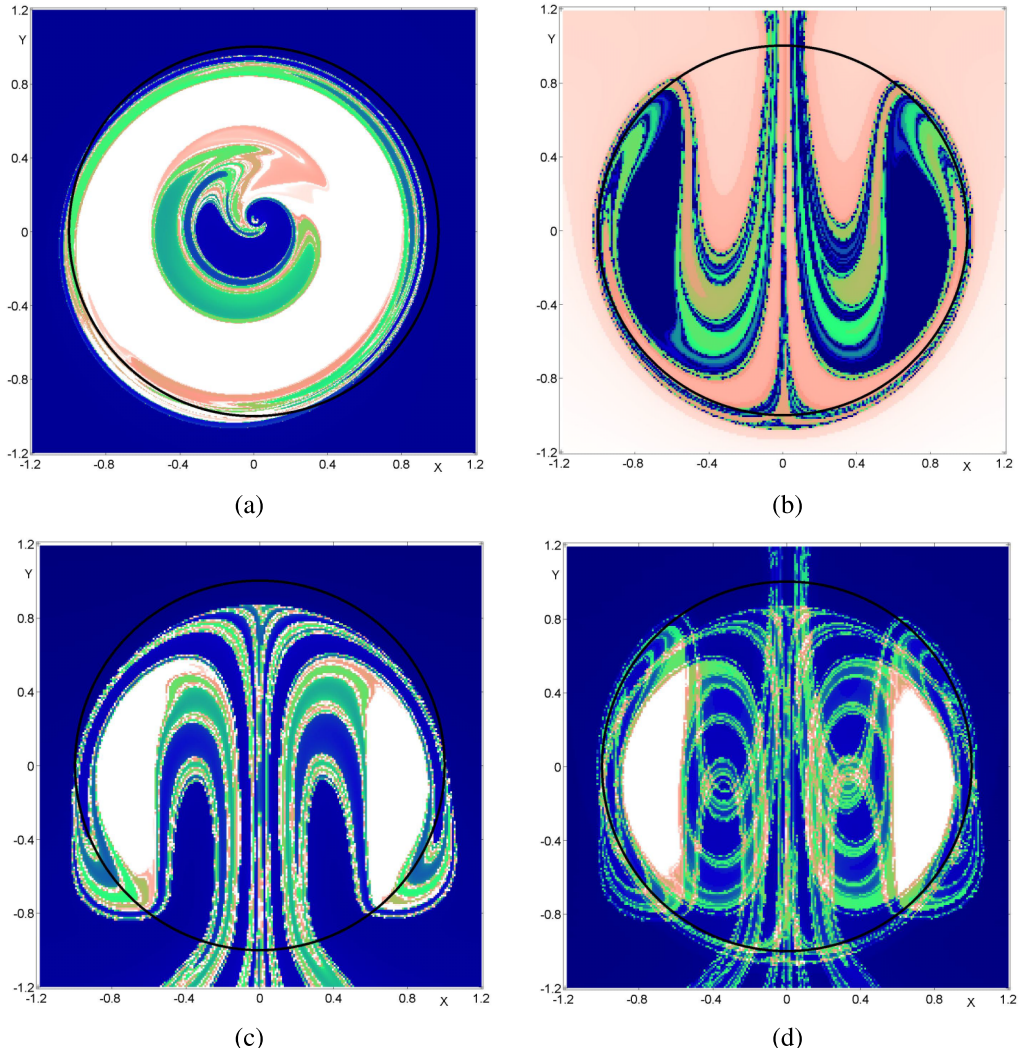


FIG. 4. Lagrangian results at two tilt-angles. Cross-sectional view at  $\theta_{\text{tilt}} = 48^\circ$  through the great circle: downstream escape time, 4(a). The Y-Z planar slice at  $\theta_{\text{tilt}} = 0^\circ$  for the upstream entry time, 4(b); downstream escape time, 4(c); and the difference between the escape time and entry time, 4(d). Lighter colors represent longer times to reach the entry plane ( $z = -2$ ) or the escape plane ( $z = +2$ ). Darker colors represent shorter times. Lobes can be seen by the grouping of regions in the escape-entry figure. (a) Plane  $z = 0$ ,  $\theta_{\text{tilt}} = 48^\circ$ . (b) Plane  $\phi = 0^\circ$ ,  $\theta_{\text{tilt}} = 0^\circ$ . (c) Plane  $\phi = 0^\circ$ ,  $\theta_{\text{tilt}} = 0^\circ$ . (d) Plane  $\phi = 0^\circ$ ,  $\theta_{\text{tilt}} = 0^\circ$ .

the DSD shows a sharp increase we attribute to the increased possibility of motion out of the plane defined by  $\theta = \text{const}$ .

The final trend we note is that for  $0.01 < \mathcal{V}_{\text{thresh}} < 100$ , the shape of the curve created was largely independent of the value chosen. Thus, our choice of  $\mathcal{V}_{\text{thresh}} = 4$  (the square of the approximate diameter of the vortex) is arbitrary, but representative. We interpret this to mean that a large portion of the fluid is either interior or exterior unmixed flow, or interior stagnant flow, where the calculated escape variance is low.

The three cases presented show the following behavior with regard to mixing. Case one (steady axisymmetric) shows mixing of fluid particles arising from shear only within the interior of the vortex and within fixed azimuthal planes. Further, fluid packets do not leave the vortex, effectively making it an unmixed case with regard to exterior flow. Case two (steady, non-axisymmetric) allows fluid particles to leave the vortex due to the strain field. Shear still plays the dominant role in mixing particles, and the broken symmetry of the vortex allows particles to change azimuthal values while the strain field allows radial changes as well as changes along the z-axis. Still present in case two

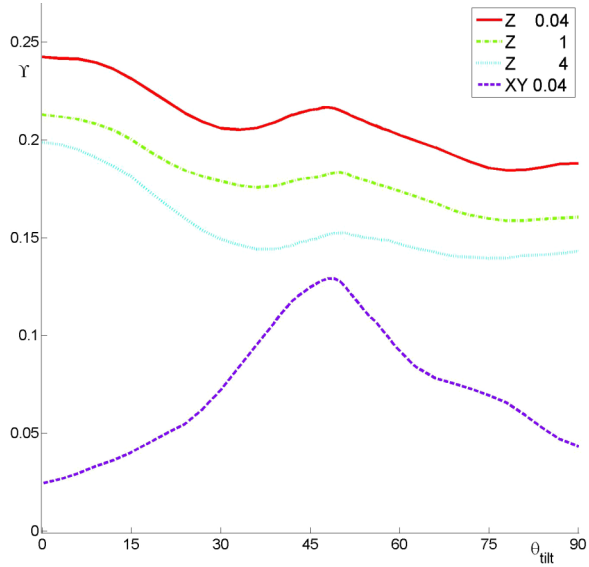


FIG. 5. Lagrangian metric,  $\Upsilon$ , shown for the DSD using only the escape time variance for the upper three contours and only the escape positional variance for the lowest contour. The variance values are compared to three different threshold values, 0.04, 1, and 4, corresponding to mild separation, separation of the sphere's radius (good), and separation by the sphere's diameter (well-separated). The lowest contour represents the downstream separation in the XY plane only, showing the effect of the tilt angles precession.

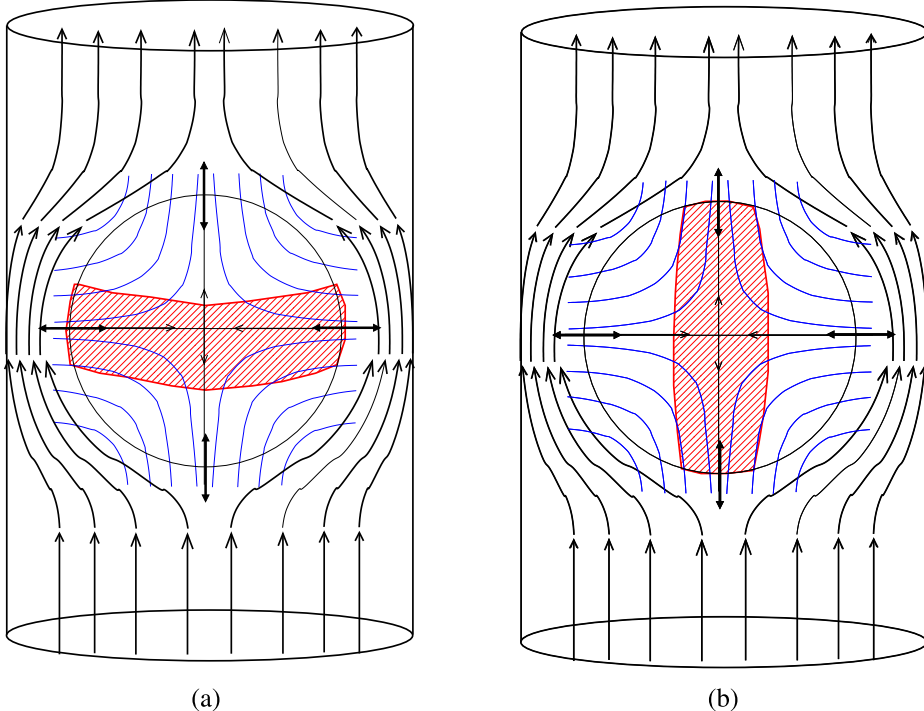


FIG. 6. Case three at the two extreme angles,  $0^\circ$  and  $90^\circ$ . The red band orthogonal to the tilt angle indicates the belted region around the sphere which entrains particles in addition to those brought into the sphere along the tilt angle axis. When  $\theta_{tilt} = 0^\circ$ , fluid particles are brought into the sphere due to the alignment of the tilt angle with the natural inclination of the exterior flow of the Hill's vortex as well as around the equator. When  $\theta_{tilt} = 90^\circ$ , the tilt angle is out of alignment with the exterior flow, still bringing in particles near the poles; however, fewer particles are entrained directly along the tilt angle, leading to fewer particles interacting with the flow inside the sphere. (a) Case 3 ( $\theta_{tilt} = 0^\circ$ ). (b) Case 3 ( $\theta_{tilt} = 90^\circ$ ).

is the plane of separation from the strain field which prevents particles from becoming fully mixed and breaks the domain into two regions. Case two then has a higher degree of mixing, but is not as fully mixed as case three. Case three (unsteady, non-axisymmetric) has the greatest degree of mixing shown due to the shear present in the vortex as well as the strain field (allowing particles to engage the exterior flow), as well as being dynamical such that a fixed separation plane does not exist, allowing the highest degree of mixing to take place. As a practical mixer, a case-three Hill's vortex residing within a pipe flow would occasionally entrain the exterior particles into the vortex, mix regions within, and then expel those particles after some time. This process is not very effective as a mixer overall as it requires particles to be pulled and later expelled from the vortex in order to mix. For these reasons, this study focused on how subdomains evolve and separate via the DSD and USD.

## B. Eulerian results

This section presents the results from the Eulerian analysis. The cross-sectional views for each EI are shown for the Y-Z plane for the whole domain investigated. Transversality,  $\alpha$ , transverse shear,  $\beta$ , mobility,  $\eta$ , and the composite EI,  $\Omega$  are shown in that order each at a tilt angle of  $\theta_{tilt} = 48^\circ$ . A three dimensional view of the Hills' vortex is shown as a sphere for transversality at a tilt angle of  $\theta_{tilt} = 48^\circ$ . Finally, the domain-averaged value for each EI versus tilt angle is shown in the last panel. The three dimensional view restricts the domain to the sphere so that a clear view of the interior can be seen, although there are important dynamics occurring just outside of the sphere boundary. The three dimensional view uses the value of the EI as a degree of transparency where peach represents a high value, hence, a more opaque pixel which then makes a smooth transition down to blue, which represents a low value, hence, a more translucent pixel.

Transversality is shown in Figures 7(a) and 7(e). The first panel shows the domain for the Y-Z plane at  $X = 0$  while the fifth panel shows the domain as a sphere using values of  $\alpha_{3D}$  as transparency. As fluid particles move downward along the polar axis, they abruptly turn at the bottom of the sphere and head upwards just inside along the edge of the spheres domain. The strain field at this point could shift particles outside of the sphere's interior flow pushing particles into the exterior flow, allowing them to leave. High values for alpha are seen at the poles of the sphere both inside and outside of the unit radius, indicating frustrated transport as well as lobe dynamics. Alpha is also shown to be high-valued in the region immediately near the interior stable vortex ring. Without perturbation, this ring would be a stagnation region; however, the undulating amplitude of the perturbation moves this stable ring near its unperturbed location, both up and down as well as in and out radially. For locations in the domain near this region, the velocity field can change direction quickly, leading to high values in transversality—illustrated as lighter colors, peach, in the figures. The transition from low angle up to high angle shows a general increase in the value of transversality. Initially shown as a darker color, blue, when the tilt angle is close to the polar axis, there is little variation in time, leading to low values in alpha. As the tilt angle sweeps towards its maximal value at  $90^\circ$ , the rotating strain field changes more of the domain, causing an increase in transversality, as shown in the figures as a rise in the intensity of the lower end of the alpha spectrum overall.

Transverse shear is shown in Figure 7(b). Regions shown in lighter colors, peach, indicate high values of the transverse shear, meaning high spatial gradients are present. The largest gradients are seen along the edge of the spherical domain, where, in the region of the exterior flow, the gradient is small, then suddenly rises within the sphere. From the interior edge of the sphere inward, the gradient becomes smaller as it approaches the stable interior region, then grows slightly moving deeper into the sphere, ultimately reaching its minimum towards the polar axis. Transverse shear is unique among EIs as it is a spatial derivative and can be calculated for each point in time. All other EIs depend on a span over time to assess their values. The figures shown depict transverse shear at the initial time for each simulation,  $t = 0$ .

Mobility is shown in Figure 7(c) in a similar fashion as  $\alpha_{3D}$  and  $\beta$ . The general features of mobility show that the exterior flow transports fluid particles well. Regions near the surface of the unit sphere can exhibit frustrated transport due to lobe dynamics. The RROC factors into mobility,

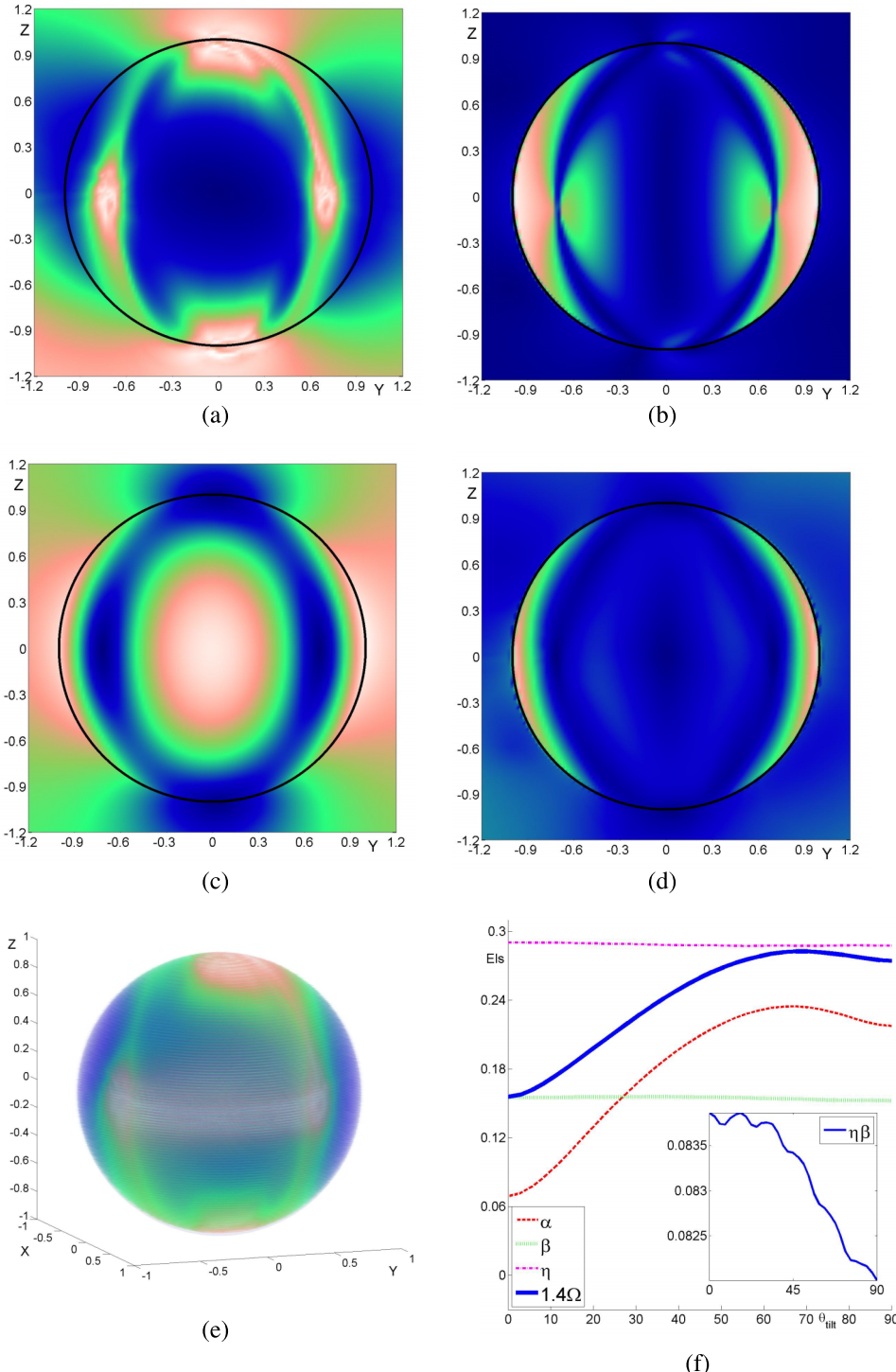


FIG. 7. Normalized EIs for transversality (7(a)), transverse shear (7(b)), mobility (7(c)), and composite EI,  $\Omega$  (7(d)) all shown for a tilt angle  $\theta_{tilt} = 48^\circ$ . Lighter colors (peach) indicate high values of the EIs, (green) represents medium values, while darker colors (blue) indicate low values. Figure 7(e) shows the transversality in full 3D across the unit sphere, while the last figure shows how the individual EIs vary with tilt angle,  $\theta_{tilt}$  averaged across a spherical domain out to a radius of 1.2 in order to include effects which engage the exterior flow. Panel 7(f) shows the domain averaged EIs,  $\langle \alpha \rangle_r$ ,  $\langle \beta \rangle_r$ ,  $\langle \eta \rangle_r$ , and  $\langle \Omega \rangle_r$ . The inset shows the  $\langle \eta \beta \rangle_r$  alone which shows the small change with respect to tilt angle; however, it also shows that the correlation to mixing is from shear, which is expected. (a) Transversality,  $\alpha$ . (b) Transverse shear,  $\beta$ . (c) Mobility,  $\eta$ . (d) Composite EI,  $\Omega$ . (e) Transversality in 3D,  $\alpha$ . (f) Domain averaged Eulerian indicators.

suppressing its value whenever a velocity field is changing quickly in time. When this occurs, the RROC value increases and the velocity integral for  $v_{fast}$  becomes the dominant term in mobility, where  $v_{fast}$  is low whenever the transport at a point is frustrated. Regions of low transport can be seen near the extrema of the polar axis, exactly where transversality is high. The combination of the two factors, low mobility at locations of high  $\alpha_{3D}$ , suppresses the effect of regions of high transversality on the composite EI,  $\Omega$ . In a similar fashion, the exterior flow shows high values of transport where transverse shear has its lowest values, suppressing the effect of transverse shear outside the unit sphere. This suggests that the regions where mobility, transversality, and transverse shear are effective are limited to three zones: exterior flow regions of moderate transversality, interior flow just inside the unit sphere where transverse shear is high, and interior flow regions away from the polar axis and away from the stable annular region. These effects on  $\Omega$  can be seen in Figure 7(d).

Figure 7(f) shows in one plot all four EIs spatially averaged over a sphere out to  $R = 1.2$ , transversality—dashed red, transverse shear—dotted green, mobility—dotted-dashed magenta line, and the composite EI,  $\langle \Omega \rangle_r$ —solid thick blue line. A multiplicative factor was added to better arrange the value in the figure. The largest change is seen in transversality, whose effect dominates the composite EI,  $\langle \Omega \rangle_r$ . The assumption in defining  $\langle \Omega \rangle_r$  is that transversality and transverse shear affect the domain equally, which may not be true. The inset shown in panel 7(f) shows the small variation versus tilt angle for the product of mobility and transverse shear. This value correlates with the Lagrangian separation metric,  $\Upsilon$ . This correlation shows that the main dynamic promoting mixing for the Hill's vortex is shear, whereas transversality indicates frustration of the flow, keeping fluid particles together, which leads to the anti-correlation between  $\langle \Omega \rangle_r$  and  $\Upsilon$ .

## VII. SUMMARY AND CONCLUSIONS: COMPARISON BETWEEN LAGRANGIAN AND EULERIAN RESULTS

The Hill's vortex is essentially a shear flow mapped into a toroid with the fastest flow moving along the edge of the sphere and along the axial symmetry axis. The addition of a time-varying strain field allows lobe dynamics to take place with the effect that entrains exterior and expels interior fluid particles.

Figure 8 shows the main results from the Lagrangian and Eulerian analyses, respectively. The Lagrangian results show that the fluid is dramatically affected by the tilt angle of the linear strain field in its ability to pull neighborhoods in the fluid apart, leading to large downstream separations, as well as the entrainment of fluid particles into the vortex, similarly separating the exterior fluid as it flows past. Lobe dynamics are seen in how the domain is segmented into a grid of regions that remain together. The largest effect from the changing strain field is observed when the symmetry of the perturbation aligns maximally with the orientation of the unperturbed flow.

The outcomes for this study include the following:

- Hill's spherical vortex plus a linear strain field was used as a test system to study 3D transport and mixing.
- The best mixing was found to be a Hill's spherical vortex with a linear strain field oriented along the symmetry axis.
- A new Lagrangian metric,  $\Upsilon$ , was developed to understand open flow separation.
- A set of Eulerian indicators were developed in 3D as well as N-dims to characterize flow which have a computational advantage of 1:97 500 over Lagrangian simulations.
- Transversality and mobility show which angles of the strain field frustrate the flow the most and lead to poor mixing.

The EIs show an effect from the linear strain field as well. The choice of the composite EI,  $\langle \Omega \rangle_r$ , anti-correlates with large values of separation distance. This effect can be explained by tracking what parts of the EIs vary with changing tilt angle,  $\theta_{tilt}$ . Across the domain, as can be seen in Figure 7(f), both the transverse shear as well as mobility vary little as the tilt angle changes. Further, transversality is suppressed by mobility, and they are competing effects in the model, such that the combination of mobility times transversality is only significant when mobility is large (outside of the domain) or when mobility is a medium value within the vortex while transversality is decreasing

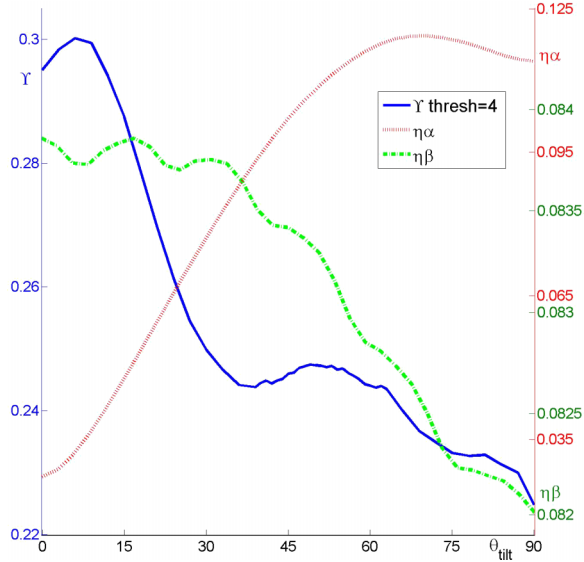


FIG. 8. Comparison of the Lagrangian metric for DSD + USD variance,  $\Upsilon$  (blue, solid) and the two EIs,  $\langle \eta\alpha \rangle_r$  (red, dotted) and  $\langle \eta\beta \rangle_r$  (green, dotted-dashed). The figure shows the domain averaged values versus tilt angle. The left vertical axis shows the values for  $\Upsilon$ , while the right vertical axis shows the ranges for the products of transversality and mobility (red) as well as transverse shear and mobility (green). The figure shows that shear, correlated to  $\Upsilon$ , is a competing effect to the transversality, anti-correlated to  $\Upsilon$ , which indicates frustration of the flow. The numerical sensitivities of the two EIs are very different which is why the composite EI,  $\Omega$ , is dominated by variation seen from transversality.

inside the sphere. In the exterior flow, both transversality and mobility grow together and show a strong dependence on tilt angle, making the composite EI grow with increasing tilt angle. The anti-correlation between EIs and Lagrangian metrics in this case makes sense as the main dynamic which leads to separation in this model is the separation achieved when the interior flow of the vortex is pulled apart along neighboring streamlines, not from sudden changes in the velocity, but from shear. As a result, when transversality increases, the flow is more frustrated and remains together more often than is pulled apart and removed into the exterior flow.

The EIs show that mobility and transverse shear correlate well spatially, however, show little variation with changing tilt angle of the perturbation. In contrast, when the flow is frustrated, mobility drops while transversality increases. Although mobility and shear show little correlation to changing tilt angle, transversality shows a high variation with the strain field, leading to the anti-correlation indicated. When the flow is the strongest and shear is the greatest, the fluid particles can separate the most and when the flow stagnates, the fluid particles remain together. The composite EI,  $\langle \Omega \rangle_r$ , shows the greatest variation with tilt angle correlated to changing alpha values, which should then anti-correlate to downstream separation.

To better understand these effects, Figure 8 shows the separate EIs,  $\langle \eta\alpha \rangle_r$  and  $\langle \eta\beta \rangle_r$  versus  $\Upsilon$ . The purpose of constructing a single composite EI, such as  $\Omega$ , is to quantify flows' features as simply as possible. Due to the large differences in sensitivity to alpha and beta, combining them without arbitrarily scaling them as well leads to alpha dominating the behavior of  $\Omega$  for the Hill's vortex. The main reason beta is suppressed in its dynamic range is that its normalization comes from dividing the values across the domain by its largest value, which suppresses it numerically. Alpha does not suffer from this problem as it is defined from  $[0^\circ, 90^\circ]$ . While a different choice for EIs can be constructed to better correlate with the Lagrangian result, this would suggest knowing in advance which properties of the flow are more significant. Addressing this issue requires knowledge of the flow field that may not be available prior to the analysis. Developing additional tools for characterizing the structure of the Eulerian sector is a continuing goal of the authors.

This study has introduced a new Lagrangian metric, the DSD and USD, for open flows. Similar in nature to a finite size Lyapunov exponent (FSLE, see Ref. 39 for a description and a list of references), where the nature of the flow is captured at a point in space—not time—the variance of

the DSD and USD measures the degree of separation of subdomains within the open flow around and inside the Hill's spherical vortex.

This analysis illustrates that a single, catch-all approach to characterizing flow using a single EI,  $\langle \Omega \rangle_r$ , is complicated. By understanding the nature of the flow—in this case, a shear flow leading to mixing—a tailor-made EI could be fashioned which correlates in the same sense as the Lagrangian metric. The important point to realize, however, is that the Eulerian sector shows correlation with the Lagrangian, suggesting that Eulerian analyses should be done in conjunction with Lagrangian, helping guide the study as the Eulerian values take considerably shorter time and indicate which portions of the domain have important dynamics for the flow under study.

## ACKNOWLEDGMENTS

The research of S.W. was supported by ONR Grant No. N00014-13-1-0329, the research of K.M. was supported by ONR Grant Nos. N00014-13-WX-2-0810 and N00014-14-WX-2-0702 as well as the Kinnear Fellowship from the USNA Foundation.

## APPENDIX A: EULERIAN INDICATORS IN N-DIMENSIONS

The three dimensional character of the Hill's vortex requires that all EIs be defined in three dimensions. In most cases, changing the former definition from two to three dimensions was trivial as the original definition was set in Cartesian coordinates, allowing an easy extension from two to three dimensions simply by adding a “z” component to each vector used in the calculation. Two of EIs, however, required more care in extending them to three dimensions, namely, transversality,  $\alpha$ , and transverse shear,  $\beta$ . Transverse shear required a redefinition as originally, it was defined by finding the gradient along the line perpendicular to the flows direction. In moving to three dimensions, the line becomes a plane and then the issue is in deciding what gradient to take within the plane normal to the flow direction. Transversality proved to be more difficult to translate into three dimensions as it is a measure of the spread of angles from the mean flow direction. In redefining the calculation to three dimensions, the issue becomes which angle should be used to consider how transverse the set of vectors is to itself.

This appendix will show that each EI can be defined not only in three dimensions but be extended into  $N$ -dimensions as well. Most of the appendix will center on the redefinition of transversality. Extending the definitions of EI from two to three dimensions was a necessary change; however, extending to  $N$  dimensions does not seem justifiable from the perspective of fluid flow, given that we live in a three dimensional world. Other data sets, however, exist that exhibit dynamics and can live in higher dimensional spaces, for example, a state vector for a stock index such as the S&P500, the pixel information from a hyper-spectral image (over many planes), and an insurance database.  $N$ -dimensional flows can exist, the question is whether these data sets have physical properties that would benefit from the application of either Lagrangian analysis or EIs.

## APPENDIX B: TRANSVERSE SHEAR, RROC, AND MOBILITY IN N-DIMENSIONS

A quick review of the definitions given in this paper for transverse shear,  $\beta$ , the *RROC*, and the mobility,  $\eta$ , shows that in each case, the definitions are applicable from two dimensions up to an arbitrarily higher number of dimensions,  $N$ . In the case of the transverse shear, the gradient operator acts on the  $N$ -dimensional velocity vector magnitude, giving the  $N$ -dimensional gradient vector,  $\rho$ . The transverse shear, given by Eq. (B3), is defined as the transverse component of  $\rho$  relative to  $\hat{v}$ ,

$$\rho(\mathbf{r}, t; \mu) = \vec{\nabla}|\mathbf{v}(\mathbf{r}, t; \mu)|, \quad (B1)$$

$$\rho(\mathbf{r}, t; \mu) \cdot \hat{v} = |\rho(\mathbf{r}, t; \mu)| \cos(\phi), \quad (B2)$$

$$\beta(\mathbf{r}, t; \mu) = |\rho(\mathbf{r}, t; \mu)| \sin(\phi), \quad (B3)$$

where  $\phi$  is the angle between  $\rho$  and  $\hat{v}$ .

Extending the definitions (Eqs. (22) and (25)) and interpretations for both the *RROC* and mobility,  $\eta$ , are trivial extensions using all  $N$  components of the velocity vector. The interpretations do not change as a result, where the *RROC* is still the relative rate of change of a vector and the mobility measures how well a position in the domain transports fluid particles away from that location.

In each of these EIs, extending from two dimensions to  $N$ -dimensions was trivial. The initial goal was simply to redefine the EIs in three dimensions; however, once it became clear that the EIs could be defined in  $N$  dimensions, the temptation to fully extend the set of definitions pushed for a redefinition of transversality as well, which proved to be more difficult.

## APPENDIX C: TRANSVERSALITY IN N-DIMENSIONS

Transversality began as a simple measure of the change in angle for a flow defined by a discrete map either in time or spatially periodic (duct flow). At each transition in the mapping of the flow, the velocity vector at a point may undergo a change in direction such that change in angle of the velocity suggests “streamline-crossing” behavior,<sup>12</sup> which has been noted as a condition which can promote mixing of the fluid. In changing from discrete maps to continuous changes in the flow, transversality was redefined as the spread of angles<sup>19</sup> around a mean angle over a window in time or space, depending on how the flow changes. When the definition of transversality is limited to two dimensions, the angle used to measure the deviation from the mean is the polar angle defined where the mean direction is the polar axis. In extending this definition from two to three to  $N$ -dimensions, additional angles are introduced into the problem, calling into question what additional transverse structure is created by the additional degrees of freedom.

Imagine a set of velocity vectors almost aligned. The mean vector defines the polar axis for the set. The standard deviation of the angles from the mean angle is approximately the transversality. Transversality is only concerned with how much a vector is perpendicular to the mean, and as a result, the value for the standard deviation of the angles is folded to lie between [0°,90°]. By changing from two to three to  $N$  dimensions, each additional dimension adds a new angular degree of freedom. For example, a set of vectors lying uniformly distributed on the 30° cone from the polar axis has a different transversality than a set of vectors at 30° forming a cross distribution in the plane normal to the flow direction. In this case, there is an additional degree of transversality taking place among the angles lying in the normal plane. By this reasoning, a recursive formula was determined which captures the idea of transversality in  $N$ -dimensions.

### 1. SVD

The  $N$ -dimensional calculation of transversality begins by first performing a SVD of the velocity vector set formed where the tail of each vector is the origin and by taking all velocity vectors at a point in the domain from a window in time,  $t_{i-X} < t_i < t_{i+X}$ , where  $X$  represents the number of samples in time both before and after the current time. SVD simultaneously calculates the scaling factors in  $N$ -dimensions as well as the orientation of the  $N$ -dimensional ellipsoid formed by the velocity vectors. The scaling factors measure the effective size of each dimension that the vector set spans. Using the scaling factors, a parameter is formed which measures the dimension “fullness” of the velocity vector set. The recursive relationship will depend only on the polar angle given from the highest dimensional axis and the next angle given by the next largest dimensional axis. The recursive relation then suggests the form the dimension fullness parameter should take dubbed,  $D_N$ ,

$$D_N = \frac{c^2}{a \times b}, \quad (C1)$$

where  $a$ ,  $b$ , and  $c$  are the first three scaling parameters given by the SVD, equivalent to the semi-major and semi-minor axes for a  $N$ -dimensional ellipsoid and  $a \geq b \geq c$ . The first ratio  $\frac{c}{b}$  gives the oblateness value—how close the distribution resembles a sphere or a clock face, whereas the second ratio,  $\frac{c}{a}$ , gives the scale factor that is needed to measure how collapsed the vector set is in

a lower dimension. Extending this definition to the  $N$ th dimension,

$$D_N = \frac{a_{N-2}^2}{a_N \times a_{N-1}}, \quad (\text{C2})$$

where  $N$  represents the current dimension that the vector set has been reduced to; the fractions are interpreted in a similar way as before. It is worth noting that the dimension fullness parameter,  $D_N$ , is an EI itself, being a product of the velocity field only.

## 2. Transversality recursion relation

The recursive formula defining  $\alpha_N$  is

$$\alpha_N = \alpha_{\theta,N} + D_N(p_N \alpha_{\theta,N} + q_{N,M} \alpha_{N-1}), \quad (\text{C3})$$

where  $\alpha_{\theta,N}$  is the transversality for the polar angles defined for the  $N$ th dimension and  $p_N, q_{N,M}$  are admixture coefficients which are set by two normalizing cases. The highest dimension that the vector set spans is denoted by  $M$  and is identified by SVD as the “largest” dimension. Finally,  $\alpha_N$  and  $\alpha_{N-1}$  are the transversality in the  $N, N - 1$  dimensions, respectively. The form of this relationship implies that the lowest dimensions must be calculated first, then successively used to calculate the next highest dimension until  $N = M$ .

There are two values labeled as “alpha” used in this calculation,  $\alpha_{\theta,N}$  and simply  $\alpha_N$ . The first value,  $\alpha_{\theta,N}$  is the deviation of the polar angles from the mean angle, which is set along the polar axis,  $\langle \theta \rangle = 0^\circ$ . The second value,  $\alpha_N$  is the transversality for the  $N$ th dimension, which takes into account any additional contributions to transversality based on how the vectors are distributed in the lower dimensions.

The two coefficients,  $p_N, q_{N,M}$ , can be found by considering two cases used for normalization. In case one, begin with an  $N$ -dimensional coordinate axes set in the positive quadrant, then rotate the set of unit vectors such that the mean vector becomes a new polar axis. Each unit vector will be at the same polar angle in the rotated system at  $\theta \geq 45^\circ$ . For three dimensions, the polar angle of the three unit vectors is  $\theta = 54.7^\circ$ . A key feature of this set of vectors is that they have preserved their angles such that all unit vectors are still  $\theta_{ij} = 90^\circ$  with respect to each other.

Case two considers a similar vector set, rotated such that the mean vector is a new polar axis. In this case, however, the rotated unit vectors are set at  $\theta = 45^\circ$ . The angle between each of the unit vectors is now *less than*  $90^\circ$ , as they lie closer to each other, in other words, they are no longer orthogonal. For three dimensions, the angle between each vector is  $\theta_{ij} = 75.5^\circ$ . Figure 9 illustrates the polar angles for the two test cases in three dimensions. One further advantage that these two test cases have is that the order of transitions between vectors does not affect the answer for the final transversality. In case one, the final transversality is  $\alpha_N^1 = 90^\circ$  as each of the unit vectors is exactly  $90^\circ$  with respect to each other, so that any sequence of transitions between the vectors always results in the final transversality being  $90^\circ$ . Similarly, for case two, the unit vectors are equidistant from each other separated by an angle,  $\theta_{ij}$ . By a similar argument, any sequence of transitions from one unit vector to the other results in the same overall transversality,  $\alpha_N^2$ , which is less than  $90^\circ$ , where superscripts have denoted the cases.

By choosing these two cases for normalization, several values can be established that will always be constant given a particular  $N$ -dimensional case. For case one,  $\alpha_N^1$  is maximal at  $90^\circ$ . For case two, the polar  $\alpha_{\theta,N}^2$  is maximal at  $90^\circ$ . By choosing these two cases, the mixing coefficients can be found,  $[p_N, q_{N,M}]$ . In both cases, the calculation for the highest dimension differs between the two; however, by “dropping” down one dimension, accomplished by removing the highest dimension coordinate from the vector, both cases become the same shape, an  $N$ -hedral simplex.

Figures 10(a) and 10(b) illustrate the idea of a coordinate system being reduced in dimension. By taking the unit vectors defined above and simply removing the highest dimensional coordinate, a new set of  $N$  vectors is created, defined over  $N - 1$  dimensions. The structure created by lowering the dimension of a coordinate system is a set of vectors that are equally distant from each other in the lower dimension. This is best considered starting from three dimensions, then dropping down to

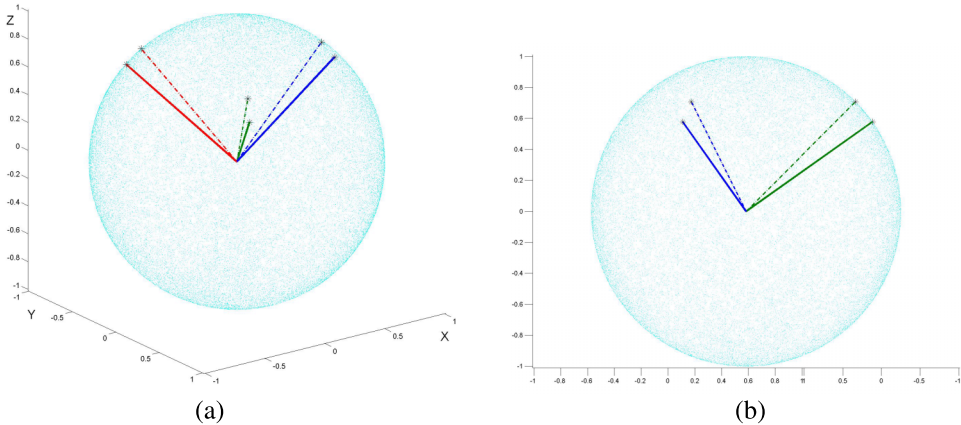


FIG. 9. Cases one (solid) and two (dashed) used in the normalization for the  $N$ -dimensional transversality calculation. In three dimensions, the unit vectors in case one are at  $\theta_{ij} = 90^\circ$ , in case two the three unit vectors lie on the  $45^\circ$  cone, making the vectors equidistant at an angle of  $\theta_{ij} = 75.5^\circ$ . (a) Cases one and two shown overlapping. (b) Cases one and two rotated to show their relative angles.

two. A coordinate set of unit vectors, equally spaced from the polar axis in three dimensions will project into two dimensions as a “peace sign,” meaning three vectors spaced apart by  $120^\circ$ . By this same argument, a four dimensional coordinate systems’ unit vectors will project into three dimensions as four vectors equally spaced apart, forming a structure similar to a methane molecule ( $CH_4$ ), shown in Figure 10(b). The angle separating each vector is  $109.5^\circ$ , known as the dihedral angle commonly used in chemistry. Higher dimensional  $N$ -hedral angles are defined as  $\cos(\theta_N^H) = -\frac{1}{N}$ .

For the cases described here, a notation is used where the case is indicated by a superscript and the variable dependence is indicated by a subscript,  $\alpha_N^1$ , for instance. Several angles are needed to define the values given in Eq. (C4), namely, the polar angle formed by each case ( $\theta_N^1, \theta_N^2, \theta_N^H$ ), the angle between any of the vectors ( $\theta_{ij,N}^1, \theta_{ij,N}^2, \theta_{ij,N}^H$ ), the polar transversality ( $\alpha_{\theta,N}^1, \alpha_{\theta,N}^2, \alpha_{\theta,N}^H$ ), and the transversality ( $\alpha_N^1, \alpha_N^2, \alpha_N^H$ ). The operator,  $\hat{\mathcal{F}}_1$ , folds angles from  $[0^\circ-180^\circ]$  about  $90^\circ$  and  $\hat{\mathcal{F}}_2$  folds angles from  $[0^\circ-90^\circ]$  about  $45^\circ$ . The angles, dimension parameters, and transversality are defined as

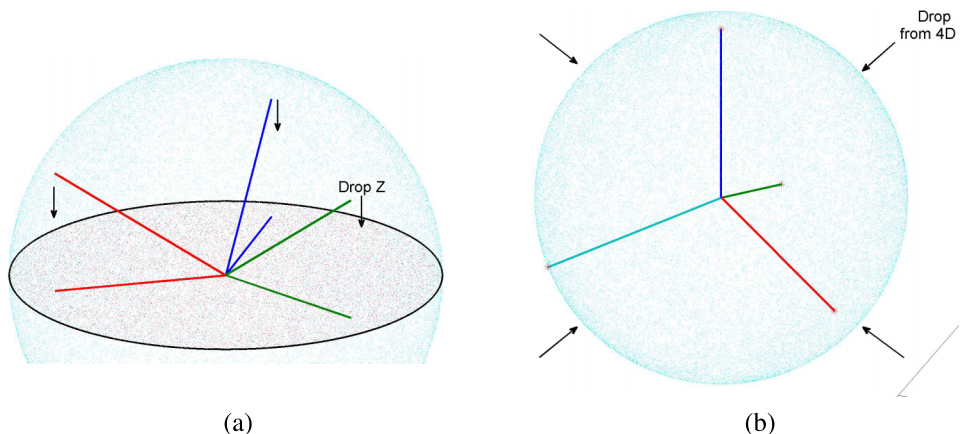


FIG. 10. Illustration of how a set of vectors is reduced in dimension. By dropping the coordinate along the polar axis, the new set of vectors is reduced to a lower structure. (a) “Dropping” dimensions for cases one or two from 3D down to 2D, forming the “peace” symbol inside the great circle. (b) Dropping dimensions from the 4D  $N$ -hedral simplex down to 3D, forming a shape similar to a  $CH_4$  molecule with a dihedral angle of  $109.5^\circ$ .

<u>Case 1</u>	<u>Case 2</u>	<u>N – hedral simplex</u>
$D_N^1 = 1$	$D_N^2 = \frac{1}{\sqrt{N-1}}$	$D_N^H = 1$
$\theta_N^1 = \cos^{-1}\left(\frac{1}{\sqrt{N}}\right)$	$\theta_N^2 = 45^\circ$	$\theta_N^H = \cos^{-1}\left(-\frac{1}{N}\right)$
$\theta_{ij,N}^1 = 90^\circ$	$\theta_{ij,N}^2 = \cos^{-1}\left(\frac{1}{2} \frac{N-2}{N-1}\right)$	$\theta_{ij,N}^H = \theta_N^H$
$\alpha_{\theta,N}^1 = 180^\circ - 2\theta_N^1$	$\alpha_{\theta,N}^2 = 90^\circ$	$\alpha_{\theta,N,M}^H = \hat{\mathcal{F}}_2\left[\sqrt{\frac{N}{M}}(180^\circ - \theta_N^H)\right]$
$\alpha_N^1 = 90^\circ$	$\alpha_N^2 = \theta_{ij,N}^2 = 75.5^\circ$	

Both normalization cases become the same structure, the  $N$  hedral simplex after dropping down from the top dimension,  $M$ . This allows the calculation to proceed identically between the two cases. Care must be taken when considering how the  $N$  hedral simplex reduces in dimension. In each case, the previous higher dimensional polar axis is reduced to zero. The calculation of transversality computes the mean variance of angles from the new polar axis. The vectors which have been reduced to zero are still present in the calculation; however, they only contribute by keeping the total number of vectors at  $M$  and not  $N$ , the current number of dimensions. For this reason,  $\alpha_{\theta,N,M}^H$  which leads to the second coefficient,  $q_{N,M}$  also depends on both  $M$  and  $N$ . Although not proven in the above equations, the value for the dimension parameter,  $D_N$  is identically one for case one and the  $N$  hedral simplex and  $\frac{1}{\sqrt{N-1}}$  for case two.

Starting from Eq. (C4) and writing out the two cases, solving for the coefficients is straight forward,

$$\alpha_N^1 = \alpha_{\theta,N}^1 + D_N^1 (p_N \alpha_{\theta,N}^1 + q_{N,M} \alpha_{N-1,M}^H), \quad (\text{C4})$$

$$\alpha_N^2 = \alpha_{\theta,N}^2 + D_N^2 (p_N \alpha_{\theta,N}^2 + q_{N,M} \alpha_{N-1,M}^H), \quad (\text{C5})$$

$$\alpha_{N,M}^H = \alpha_{\theta,N}^H + D_N^H (p_N \alpha_{\theta,N}^H + q_{N,M} \alpha_{N-1,M}^H), \quad (\text{C6})$$

$$p_N = \sqrt{N-1} \left[ \frac{90^\circ - \theta_{ij,N}^2}{90^\circ - 2\theta_N^1} \right] - 1, \quad (\text{C7})$$

$$q_{N,M} = \frac{1}{\alpha_{N-1,M}^H} [90^\circ - \alpha_{\theta,N}^1 (p_N + 1)]. \quad (\text{C8})$$

By definition, the coefficients,  $p_1, p_2, q_{1,M}, q_{2,M} \equiv 0$  as there is no transversality in one dimension and only the polar transversality in two dimensions. Starting from  $N = 2, M = 3$ , the values of  $\alpha_{N,M}^H$  are calculated, each building the term needed by the next higher dimension,

$$\alpha_{1,M}^H = 0, \quad (\text{C9})$$

$$\alpha_{2,M}^H = \alpha_{\theta,2,M}^H, \quad (\text{C10})$$

$$\alpha_{3,M}^H = (1 + D_3^H p_3) \alpha_{\theta,3} + D_3^H q_{3,M} \alpha_{2,M}^H, \quad (\text{C11})$$

$$\alpha_{4,M}^H = (1 + D_4^H p_4) \alpha_{\theta,4} + D_4^H q_{4,M} \alpha_{3,M}^H, \quad (\text{C12})$$

$$\vdots \quad (\text{C13})$$

$$\alpha_{N,M}^H = (1 + D_N^H p_N) \alpha_{\theta,N} + D_N^H q_{N,M} \alpha_{N-1,M}^H. \quad (\text{C14})$$

The definitions of  $D_N^H$  and  $q_{N,M}$  reduce the formula for the  $N$  hedral simplex to

$$\alpha_{N,M}^H = \hat{\mathcal{F}}_1 [90^\circ + (1 + p_N) (\alpha_{\theta,N,M}^H - \alpha_{\theta,N}^1)]. \quad (\text{C15})$$

Using the formulas presented, calculated values for both  $p_N$  and  $q_{N,M}$  are given in Table I.

TABLE I. Calculated values for the coefficients  $q_{N,M}$  and  $p_N$  needed for the evaluation of transversality,  $\alpha_N$ . In the table,  $M$  represents the largest dimension the vector set spans and  $N$  represents the dimension for which the calculation is performed. The coefficients,  $q_{N,M}$  and  $p_N$ , are admixture constants based on the normalization cases one and two.

N \ M	$q_{N,M}$								$p_N$
	3	4	5	6	7	8	9	10	
3	2.00	1.93	2.16	2.37	2.56	2.74	2.90	3.06	-2.05
4	0	2.05	1.75	1.97	2.19	2.15	2.00	1.90	-2.12
5	0	0	2.10	1.78	1.84	2.04	2.25	2.46	-2.19
6	0	0	0	2.14	1.81	1.74	1.93	2.12	-2.26
7	0	0	0	0	2.17	1.85	1.66	1.84	-2.32
8	0	0	0	0	0	2.20	1.87	1.67	-2.38
9	0	0	0	0	0	0	2.22	1.90	-2.44
10	0	0	0	0	0	0	0	2.24	-2.49

### 3. Calculation of transversality in N-dimensions

The following steps describe how to calculate the  $N$ -dimensional transversality.

1. Collect a set of  $n$ -dimensional vectors ( $\mathbf{v}$ ), where  $N_v$  denotes the size of the vector set and  $N$  denotes the number of dimensions that define the vectors.
2. Normalize the vector set to the unit  $N$ -dimensional sphere.
3. Calculate the SVD of the vector set.
4. Rotate the vector set by the rotation matrix obtained from SVD to obtain a new set of vectors,  $\mathbf{v}' = U^\top \mathbf{v}$ , whose components are given by  $v'_i$ , where  $i = 1, \dots, N$ .
5. From the scaling matrix obtained from SVD, compute the set of dimension parameters,  $D_N = \frac{a_{N-2}^2}{a_N \times a_{N-1}}$ .
6. Calculate the polar angle transversality,  $\alpha_{\theta,N}$ , as follows.
  - Define the polar angle in the  $N$ th dimension for the  $i$ th vector:  $\theta_i = \cos^{-1} \left( \frac{v'_N}{\sqrt{\sum_{j=1}^N v_j'^2}} \right)$ .
  - Fold the polar angles to be less than  $90^\circ$ :  $\tilde{\theta}_i = \hat{\mathcal{F}}_1[\theta_i]$ .
  - Calculate the variance of the folded angle:  $\mathcal{V}(\tilde{\theta}_i) = \frac{1}{N_v} \sum_{i=1}^{N_v} (\tilde{\theta}_i - 0^\circ)^2$ .
  - Calculate the standard deviation of the variance:  $\sigma(\tilde{\theta}) = \sqrt{\mathcal{V}(\tilde{\theta}_i)}$ .
  - Fold the rms value about  $45^\circ$  and normalize to  $90^\circ$  to obtain the polar transversality:  $\alpha_{\theta,N} = 2\hat{\mathcal{F}}_2[\sigma(\tilde{\theta})]$ .
  - The whole calculation can be summarized in one formula:  $\alpha_{\theta,N} = 2\hat{\mathcal{F}}_2 \left[ \sqrt{\frac{1}{N_v} \sum_{i=1}^{N_v} (\hat{\mathcal{F}}_1[\theta_i] - 0^\circ)^2} \right]$ .

7. From the rotated set of vectors,  $\mathbf{v}'$ , create subsets of vectors by removing the highest dimension's coordinate, creating a set of  $N_v$  vectors for each lower dimension,  $\tilde{\mathbf{v}}'_n$ , where  $n = 1, \dots, N-1$ .
8. Using the recursive formula:  $\alpha_N = (1 + D_N p_N) \alpha_{\theta,N} + D_N q_{N,M} \alpha_{N-1}$ , begin calculating the transversality from the lowest dimensions upwards until reaching the highest dimension,  $N$ . In each of the lower dimensions, the set of vectors used to calculate  $\alpha_{\theta,N}$  is based on the respective set of lower dimensional vectors,  $\tilde{\mathbf{v}}'_N$ ,

$$\begin{aligned}
\alpha_1 &= 0, \\
\alpha_2 &= \alpha_{\theta,2}, \\
\alpha_3 &= (1 + D_3 p_3) \alpha_{\theta,3} + D_3 q_{3,M} \alpha_2, \\
\alpha_4 &= (1 + D_4 p_4) \alpha_{\theta,4} + D_4 q_{4,M} \alpha_3, \\
&\vdots \\
\alpha_N &= (1 + D_N p_N) \alpha_{\theta,N} + D_N q_{N,M} \alpha_{N-1}.
\end{aligned}$$

- <sup>1</sup> H. Aref, "The development of chaotic advection," *Phys. Fluids* **14**(4), 1315–1325 (2002).
- <sup>2</sup> V. I. Arnold, "Sur la topologie des écoulements stationnaires des fluides parfaits," *C. R. Acad. Sci. Paris A* **261**, 17 (1965).
- <sup>3</sup> M. Hénon, "Sur la topologie des lignes courant dans un cas particulier," *C. R. Acad. Sci. Paris A* **262**, 312 (1966).
- <sup>4</sup> A. Acrivos, H. Aref, and J. M. Ottino, IUTAM International Symposium on Fluid Mechanics of Stirring and Mixing, *La Jolla*, [Phys. Fluids A, Part 2 **3**(5) (1991)].
- <sup>5</sup> H. Aref and M. S. El Naschie, *Chaos Applied to Fluid Mixing* [Chaos, Solitons Fractals **4**(6) (1994)].
- <sup>6</sup> A. Babiano, A. Provenzale, and A. Vulpiani, Chaotic Advection, Tracer Dynamics, and Turbulent Dispersion Proceedings of the NATO Advanced Research Workshop and EGS Topical Workshop on Chaotic Advection, *Conference Centre Sereno di Gavo, Italy*, [Physica D **76** (1994)].
- <sup>7</sup> D. Beigie, A. Leonard, and S. Wiggins, "Invariant manifold templates for chaotic advection," *Chaos, Solitons Fractals* **4**(6), 749–868 (1994).
- <sup>8</sup> J. M. Ottino, *The Kinematics of Mixing: Stretching, Chaos, and Transport* (Cambridge University Press, Cambridge, England, 1989), Reprinted 2004.
- <sup>9</sup> R. M. Samelson and S. Wiggins, *Lagrangian Transport in Geophysical Jets and Waves: The Dynamical Systems Approach* (Springer-Verlag, New York, 2006).
- <sup>10</sup> R. Sturman, J. M. Ottino, and S. Wiggins, *The Mathematical Foundations of Mixing*, Cambridge Monographs on Applied and Computational Mathematics (Cambridge University Press, 2006), Vol. 22.
- <sup>11</sup> S. Wiggins and J. Ottino, "Foundations of chaotic mixing," *Philos. Trans. R. Soc., A* **362**(1818), 937–970 (2004).
- <sup>12</sup> J. M. Ottino, "Mixing, chaotic advection, and turbulence," *Annu. Rev. Fluid Mech.* **22**, 207–254 (1990).
- <sup>13</sup> E. Villermaux, A. D. Stroock, and H. A. Stone, "Bridging kinematics and concentration content in a chaotic micromixer," *Phys. Rev. E* **77**, 015301(R) (2008).
- <sup>14</sup> J. M. Ottino and S. Wiggins, "Designing optimal micromixers," *Science* **305**, 485–486 (2004).
- <sup>15</sup> S. Wiggins, "Chaos in the dynamics generated by sequences of maps, with applications to chaotic advection in flows with aperiodic time dependence," *ZAMP* **50**, 585–616 (1999).
- <sup>16</sup> R. Sturman and S. Wiggins, "Eulerian indicators for predicting and optimizing mixing quality," *New J. Phys.* **11**, 075031 (2009).
- <sup>17</sup> K. McIlhany and S. Wiggins, "Optimizing mixing in channel flows: Kinematic aspects associated with secondary flows in the cross-section," *Microfluid. Nanofluid.* **10**, 249–262 (2011).
- <sup>18</sup> K. L. McIlhany, D. Mott, E. Oran, and S. Wiggins, "Optimizing mixing in lid-driven flow designs through predictions from Eulerian indicators," *Phys. Fluids* **23**, 082005 (2011).
- <sup>19</sup> K. L. McIlhany and S. Wiggins, "Eulerian indicators under continuously varying conditions," *Phys. Fluids* **24**(7), 073601 (2012).
- <sup>20</sup> A. M. Mancho, D. Small, and S. Wiggins, "A tutorial on dynamical systems concepts applied to Lagrangian transport in oceanic flows defined as finite time data sets: Theoretical and computational issues," *Phys. Rep.* **437**(3–4), 55 (2006).
- <sup>21</sup> S. Wiggins, "The dynamical systems approach to Lagrangian transport in oceanic flows," *Annu. Rev. Fluid Mech.* **37**, 295–328 (2005).
- <sup>22</sup> M. R. Bringer, C. J. Gerdts, H. Song, J. D. Tice, and R. F. Ismagilov, "Microfluidic systems for chemical kinetics that rely on chaotic mixing in droplets," *Philos. Trans. R. Soc., A* **362**, 1087–1104 (2004).
- <sup>23</sup> R. O. Grigoriev, "Chaotic mixing in thermocapillary-driven microdroplets," *Phys. Fluids* **17**, 033601 (2005).
- <sup>24</sup> R. H. Liu, M. A. Stremler, K. V. Sharp, M. G. Olsen, J. G. Santiago, R. J. Adrian, H. Aref, and D. Beebe, "Passive mixing in a three-dimensional serpentine microchannel," *J. Microelectromech. Syst.* **9**(2), 190–197 (2000).
- <sup>25</sup> J. M. Ottino and S. Wiggins, "Introduction: Mixing in microfluidics," *Philos. Trans. R. Soc., A* **362**(1818), 923–935 (2004).
- <sup>26</sup> F. Sotiropoulos, Y. Ventikos, and T. C. Lackey, "Chaotic advection in three-dimensional stationary vortex-breakdown bubbles: Si'l'nikov's chaos and the devil's staircase," *J. Fluid Mech.* **444**, 257–297 (2001).
- <sup>27</sup> M. A. Stremler, F. Haselton, and H. Aref, "Designing for chaos: Applications of chaotic advection at the microscale," *Philos. Trans. R. Soc., A* **362**(1818), 1019–1036 (2004).
- <sup>28</sup> A. D. Stroock, S. K. W. Dertinger, A. Ajdari, I. Mezic, H. A. Stone, and G. M. Whitesides, "Chaotic mixer for microchannels," *Science* **295**, 647–651 (2002).
- <sup>29</sup> T. Ward and G. M. Homsy, "Electrohydrodynamically driven chaotic mixing in a translating drop," *Phys. Fluids* **13**(12), 3521–3525 (2001).
- <sup>30</sup> X. Xu and G. M. Homsy, "Three-dimensional chaotic mixing inside drops driven by a transient electric field," *Phys. Fluids* **19**(1), 3102 (2007).
- <sup>31</sup> G. O. Fountain, D. V. Khakhar, and J. M. Ottino, "Visualization of three-dimensional chaos," *Science* **281**, 683–686 (1998).
- <sup>32</sup> R. S. MacKay, "Transport in 3d volume-preserving flows," *J. Nonlinear Sci.* **4**, 329–354 (1994).
- <sup>33</sup> I. Mezic and S. Wiggins, "On the integrability and perturbation of three-dimensional fluid flows with symmetry," *J. Nonlinear Sci.* **4**, 157–194 (1994).

- <sup>34</sup> G. K. Batchelor, *An Introduction to Fluid Dynamics* (Cambridge University Press, 1967).
- <sup>35</sup> V. Rom-Kedar, A. Leonard, and S. Wiggins, “An analytical study of transport, mixing, and chaos in an unsteady vortical flow,” *J. Fluid Mech.* **214**, 347–394 (1990).
- <sup>36</sup> V. Rom-Kedar and S. Wiggins, “Transport in two-dimensional maps,” *Arch. Ration. Mech. Anal.* **109**(3), 239–298 (1990).
- <sup>37</sup> M. Branicki and S. Wiggins, “An adaptive method for computing invariant manifolds in non-autonomous, three-dimensional dynamical systems,” *Physica D* **238**(16), 1625–1657 (2009).
- <sup>38</sup> A. M. Mancho, S. Wiggins, J. Curbelo, and C. Mendoza, “Lagrangian descriptors: A method for revealing phase space structures of general time dependent dynamical systems,” *Commun. Nonlinear Sci. Numer. Simul.* **18**(12), 3530–3557 (2013).
- <sup>39</sup> M. Branicki and S. Wiggins, “Finite-time Lagrangian transport analysis: Stable and unstable manifolds of hyperbolic trajectories and finite-time Lyapunov exponents,” *Nonlinear Processes Geophys.* **17**, 1–36 (2010).